공학박사 학위논문

A Study on Thermal Behavior of Lightweight Carbon/Polymer Composites

탄소 고분자 경량 복합재료의 열 전달 거동에 관한 연구

2017년 8월

서울대학교 대학원
재료공학부
박 성 열

Abstract

To investigate thermal behavior of lightweight carbon/polymer composites and to explore the potential applications of composites are the main topics of this study. Present study dealt with unique experimental results such as synergistic improvement in thermal conductivity of multiphase composites and enhancement in surface hardness of graphene aerogel-based composites. To explore dominant factors determining the thermal conductivity of the carbon/polymer composites is also an important goal of this study.

In Chapter 2, the thermal conductivity of composites with a polyphenylene sulfide (PPS) matrix and a mixture of boron nitride (BN) powder and multi-wall carbon nanotube (MWCNT) fillers was investigated. Synergistic improvement in thermal conductivity of the composite was obtained by introducing a combination of BN and MWCNT. The improvement of thermal conductivity was strongly depended on surface treatments of the MWCNTs, such as hydrogen peroxide and acid treatments. The thermal conductivity of the composite was affected by the interaction and interfacial thermal resistance between the PPS matrix and the BN filler. The interfacial thermal resistance of PPS/BN/MWCNT composites was investigated quantitatively by finite element method. The highest thermal conductivity was 1.74 W/m·K achieved by the composite with 1 wt% MWCNT that had been treated by hydrogen peroxide., This result indicated that we successfully fabricated a pelletizable, injection moldable, thermally conductive carbon/polymer composite, considering the specific thermal conductivity of the prepared composite.

In Chapter 3, three-dimensional carbon nanomaterial reinforced composite aerogel was fabricated using a freeze-drying method. Graphene nanoplatelets (GNPs) were used as the reinforcement and poly vinyl alcohol (PVA) as the organic binding material to produce the composite aerogel. Two different methods were employed to control the internal structure of the aerogel: a variation of solvent composition and

the formation of cross-linking. The internal structure of the aerogel was affected by the types and composition of the solvent. In addition, the subsequent cross-linking of the aerogel influenced the morphology and physical properties. This study is expected to provide a simple and efficient way to control the internal structure and resulting properties of the GNP aerogel.

In Chapter 4, the thermal and electrical conductivity of composites with a graphene aerogel and an epoxy matrix were investigated. We fabricated a core-shell structured composites with the graphene aerogel core and the epoxy/graphene composite shell in order to enhance the poor surface hardness of graphene aerogel, resulting in increased resistance of graphene aerogel to the external forces. The thermal conductivity of the core-shell structured epoxy/rGO composites was 0.077 W/m·K which is similar to that of thermal insulating materials. On the other hand, the electrical conductivity of composite was found to exhibit 0.5 S/m which is almost 10 orders of magnitude higher than that of neat epoxy. This result indicated that carbon/polymer composites have a great potential in numerous engineering applications.

Keyword: carbon/polymer composite, thermal conductivity, interfacial thermal resistance, three-dimensional pathway, carbon aerogel, core-shell structure

Student Number: 2008-20644

Contents

List of Figures

List of Tables

Chapter 1. Introduction

1.1. Carbon Nanomaterials

Carbon nanomaterials (*e.g.*, graphene, carbon nanotube and fullerene) have been extensively studied due to their extraordinary properties and numerous applications [1, 2]. Carbon nanomaterials can be classified by their shape and dimension. The graphene is two-dimensional carbon nanosheet and a new fabrication method with mechanical exfoliation of bulk graphite was recently explored for the single layer graphene [3]. The carbon nanotube is the one-dimensional, atomic-scaled carbon cylinder structure with very high aspect ratio, and was discovered by Iijima in electrical arc experiments [4]. The single wall carbon nanotube can be expressed as cylinder-like rolled form of a single layer graphene sheet. The fullerene is a zero-dimensional form of carbon nanomaterial having a variety of structure including hollow sphere, ellipsoid and *etc*. Fig. 1.1 shows the dimension of carbon nanomaterials.

The outstanding mechanical property of these carbon nanomaterials is attributed to the covalent carbon-carbon bonding and their hexagonal crystal structure [5, 6]. The extraordinary thermal conductivity of carbon nanomaterials is resulted from a long mean free paths of a sp^2 orbital hybridization in the hexagonal structure [7]. Moreover, carbon nanomaterials have outstanding electrical properties such as electrical conductivity and carrier density, which were attributed to the formation of electron cloud at the pi-pi orbitals of carbon nanomaterials [8].

Both CNT and graphene have proved that they have promising future for various applications including the gas sensors [9-11], battery electrode [12-14], thermal interface material [15-18] and thermoelectric devices [19, 20]. However, the structural difference between CNT and graphene determines their properties and the fields of applications. From the perspective of electrical conductivity, the CNT possesses

more advantage than the graphene. The electrical conductivity of the graphene was rapidly dropped to the ~10^3 S/m with the effect of the defects including disordered carbon and agglomeration of graphene layers. Considering the value of ~10^6 S/m for electrical conductivity of CNTs, the capability of the graphene to the electrical fields is limited. However, the theoretical specific surface area of graphene is twice larger than that of CNT due to the two-dimensional structure of the graphene. This indicates that active sites on the graphene surface are more abundant than those of CNT, which can enhance the energy density and specific capacitance of carbon electrode [21].

Due to the remarkable properties of carbon nanomaterials, the potential application of carbon nanomaterials is popular in the carbon/polymer composites. Several scientists have reported that the mechanical properties of MWCNT/polymer composite were enhanced by adding the small amount of MWCNTs [22-25]. A low percolation threshold of the electrical conductivity of less than 1.0 wt% CNT or graphene loading were observed in the carbon/polymer composites [26, 27].

Thermal conductivities of carbon/polymer composites were also studied by many researchers [28, 29]. A variety of analytical models were used to predict the thermal conductivity of carbon/polymer composite [30-33]. However, thermal conductivity enhancement of carbon/polymer composites was not significant compared with the thermal conductivity expected by theoretical calculations [26, 27]. Although various attempts were tried in order to improve the thermal conductivity of carbon/polymer composites, fabricating the highly thermally conductive composite with a good processability is still challenging task [23, 34].

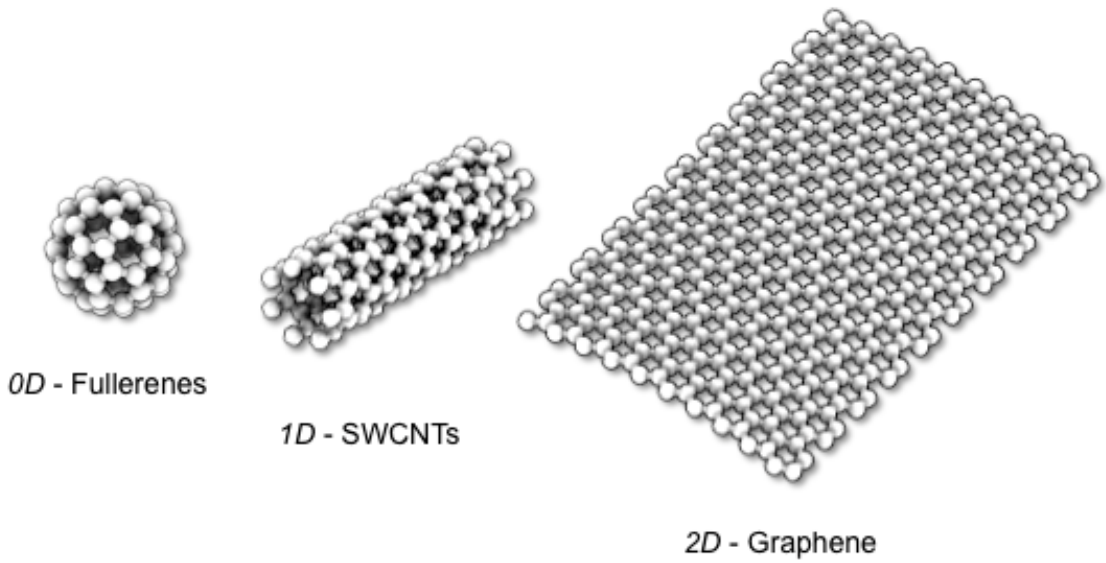

Figure 1.1 Dimensions of carbon nanomaterials.

1.2. Factors Affecting Thermal Conductivity

In order to investigate the effective thermal conductivity of the carbon/polymer composite, we need to understand a percolation theory. The percolation, used frequently to explain electrical conduction in composite medium, is the pathway of an carriers through a randomly structured composite medium where the carriers can pass through some areas more easily than the other areas of medium [35]. A schematic diagram of visualized percolation phenomenon is shown in Fig 1.2. One way to express the percolation phenomenon is as a forest fire, assuming that fire can be spread only to the nearest tree. The fire spreads quickly through the dry area, but the speed of fire was decreased in the wetter area. Therefore, the fire goes through a pathway avoiding the wetter areas. This percolation theory, which was used to predict the effective thermal conductivity of composites, also has been studied by many researchers. However, thermal behavior of composites cannot be explained by using percolation theory only [36]. Moreover, reduced thermal conductivity of CNT/polymer composite with high CNT loading was reported in the literatures [37].

Interfacial thermal resistance, also called thermal boundary resistance or Kapitza resistance, is due to the mismatch in the properties between the fillers and the matrix, was firstly measured by Kapitza in 1941 [38]. The fillers and the matrix are of different materials, having different acoustic properties such as Debye temperatures, frequencies and speeds of sound, inducing the phonon scattering at the interface between the fillers and the matrix [36]. It is noting that the interfacial thermal resistance is more important than the thermal contact resistance which was owing to the roughness of surfaces in contact, since the surface roughness of a nano-size particle is insignificant for determining the thermal properties of composites. Moreover, thermal interfacial resistance is presented even in the case of perfect contact between the filler and the matrix. Therefore, the interfacial thermal resistance is more dominant to determine thermal conductivity of

composite than the thermal contact resistance. The interfacial thermal resistance is also related to the temperature discontinuity between the fillers and the matrix, inducing resistance to the transfer of phonons. When the loading of filler is increased, this resistance to the transport of phonons would be significant, thus reducing the effective thermal conductivity of composite [39]. The expression for thermal boundary resistance (R_b) is given for

$$R_b = \frac{\Delta T}{Q}, \tag{1.1}$$

where Q is the applied heat flux and $\Delta \mathrm{T}$ is the observed temperature difference. Considering the remarkable large discrepancy of acoustic properties between the carbon filler and the polymer matrix, relatively low thermal conductivity of carbon/polymer composites is attributed to the interfacial thermal resistance. [40].

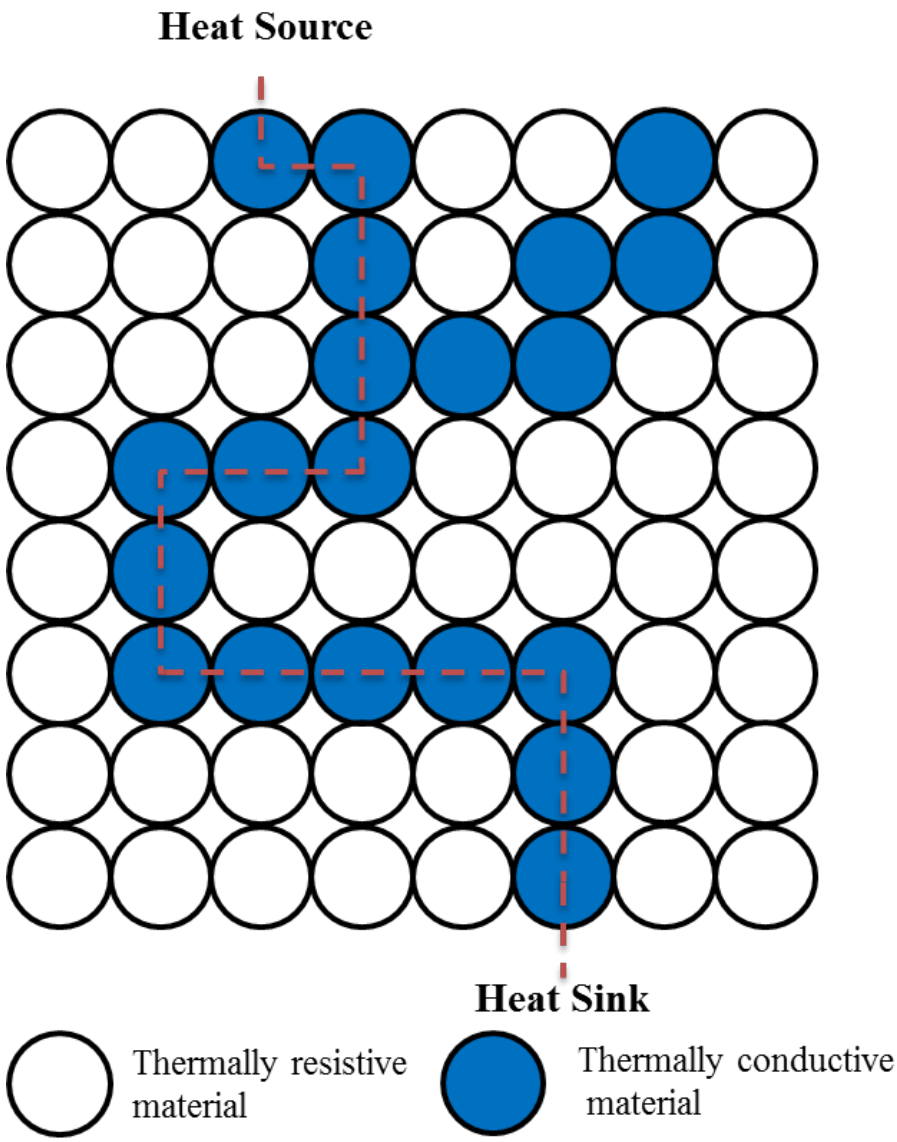

Figure 1.2 A scheme of heat transfer improvement, 2-phase composite materials, due to the percolation. Thermally conductive materials, forming a continuous chain from the heat source to the heat sink.

1.3. Applications of Carbon/Polymer Composite

The lightweight materials have attracted a considerable attention in recent years. According to a study done at IFEU institute, a weight saving of 100 kg in transportation cars compensated by using lightweight materials for automotive parts, resulting in an average saving of 0.35 liter of petrol per 100 km. CO_2 emissions are also reduced by about 10g/km in relation to the total fuel supply [41]. These results indicated that polymer composites are a lightweight alternative to metal and its alloys. The mechanical properties of polymer composites can be enhanced by adding a small amount of carbon nanomaterials which were reported in the several literatures [22-25]. Therefore, carbon/polymer composites are good candidate materials for various engineering applications needed the lightweight and high mechanical property.

In recent decades, the demands of thermally conductive polymers have been increased because high thermal conductivity is needed for fast dissipation of heat in electronics. Furthermore, electrical insulating property of polymer composites was also required due to the safety during the operation of electronic device. Thus, electronic insulating and thermally conductive polymer composites can be applicable to the various fields such as electronic packaging, heat sink in the engineering device and circuit board housing [42-44].

On the other hands, the physical properties can be manipulated by controlling the structure and the composition of carbon/polymer composites. In order to expand the application of carbon/polymer composites, comprehensive and systematic studies for investigating the specific properties of carbon/polymer composites are needed.

.

1.4. Objectives

The main objective of present study is to investigate the thermal behavior of lightweight carbon/polymer composites and the role of factors for determining the effective thermal conductivity of carbon/polymer composite. This study dealt with unique experimental results; a synergistic improvement of thermal conductivity of PPS/BN/MWCNT composite and extraordinary thermal and electrical property of the core-shell epoxy/rGO composite. Moreover, numerical simulation was also carried out for theoretical investigation. Another objective of this study is to explore potential applications of carbon/polymer composites.

The factors contributing to the synergistic improvement of the PPS/BN/MWCNT composite were investigated in Chapter 2. The role of three-dimensional network was not insignificant due to the imperfect formation of heat transfer pathway. Therefore, relationship between the interfacial thermal resistance and the effective thermal conductivity of composite was focused in this chapter. In order to investigate the role of interfacial interaction induced by surface treatment, finite element method was employed. Moreover, the specific thermal conductivity of PPS/BN/MWCNT composite was also compared with that of metal and commercial thermal conductive polymers.

In order to investigate the effect of three-dimensional network for determining effective thermal conductivity, the thermal conductivity of lightweight GNP/PVA composite aerogel was measured by modified source plane method. The GNP/PVA aerogels were prepared by freeze-drying method. Thus, three-dimensional network in GNP/PVA aerogel was changed by controlling the GNP/PVA weight ratio, the composition of solvent, and the chemical treatment to PVA. Mechanical property and stability in the aqueous environment of GNP/PVA aerogels were also investigated for exploring the potential application of carbon/polymer composite aerogels. Advanced PCM composed of PEG and GNP/PVA aerogel is a newly suggested application of carbon/polymer composite

aerogel in Chapter 3.

To overcome the poor surface hardness of carbon aerogel, core-shell structured composite was fabricated by using the impregnation technique in Chapter 4. Although the core shell structure of epoxy and rGO aerogel was constructed, the extraordinary properties of the rGO aerogel such as low thermal conductivity, high electrical conductivity and low density were maintained. Thermal behavior of this unique composite was also investigated by a theoretical approach.

1.4. References

[1] Geim AK, Novoselov KS. *The rise of graphene*. Nature materials. 2007;6(3):183-91.

[2] Saxena S, Tyson TA. *Interacting quasi-two-dimensional sheets of interlinked carbon nanotubes: a high-pressure phase of carbon.* ACS nano. 2010;4(6):3515-21.

[3] Novoselov KS, Geim AK, Morozov SV, Jiang D, Zhang Y, Dubonos SV, et al. *Electric field effect in atomically thin carbon films.* science. 2004;306(5696):666-9.

[4] Iijima S. *Helical microtubules of graphitic carbon.* nature. 1991;354(6348):56-8.

[5] Yu M-F, Lourie O, Dyer MJ, Moloni K, Kelly TF, Ruoff RS. *Strength and breaking mechanism of multiwalled carbon nanotubes under tensile load. Science*. 2000;287(5453):637-40.

[6] Lee C, Wei X, Kysar JW, Hone J. *Measurement of the elastic properties and intrinsic strength of monolayer graphene*. science. 2008;321(5887):385-8.

[7] Berber S, Kwon Y-K, Tománek D. *Unusually high thermal conductivity of carbon nanotubes.* Physical review letters. 2000;84(20):4613.

[8] Cooper DR, D' Anjou B, Ghattamaneni N, Harack B, Hilke M, Horth A, et al. *Experimental review of graphene*. ISRN Condensed Matter Physics. 2012;2012.

[9] Yoon HJ, Yang JH, Zhou Z, Yang SS, Cheng MM-C. *Carbon dioxide gas sensor using a graphene sheet.* Sensors and Actuators B: Chemical. 2011;157(1):310-3.

[10] Li J, Lu Y, Ye Q, Cinke M, Han J, Meyyappan M. *Carbon nanotube sensors for gas and organic vapor detection.* Nano letters. 2003;3(7):929-33.

[11] Zhang T, Mubeen S, Myung NV, Deshusses MA. *Recent progress in carbon nanotube-based gas sensors.* Nanotechnology. 2008;19(33):332001.

[12] Liu X-M, dong Huang Z, woon Oh S, Zhang B, Ma P-C, Yuen MM, et al. *Carbon nanotube (CNT)-based composites as electrode material for rechargeable Li-ion batteries: a review.* Composites Science and Technology. 2012;72(2):121-44.

[13] Reddy ALM, Shaijumon MM, Gowda SR, Ajayan PM. *Coaxial MnO2/carbon nanotube array electrodes for high-performance lithium batteries.* Nano Letters. 2009;9(3):1002-6.

[14] Wang C, Li D, Too CO, Wallace GG. *Electrochemical properties of graphene paper electrodes used in lithium batteries.* Chemistry of Materials. 2009;21(13):2604-6.

[15] Xu J, Fisher TS. *Enhancement of thermal interface materials with carbon nanotube arrays.* International Journal of Heat and Mass Transfer. 2006;49(9):1658-66.
[16] Yu A, Ramesh P, Itkis ME, Bekyarova E, Haddon RC. *Graphite nanoplatelet-epoxy composite thermal interface materials.* The Journal of Physical Chemistry C. 2007;111(21):7565-9.
[17] Shahil KM, Balandin AA. *Thermal properties of graphene and multilayer graphene: Applications in thermal interface materials.* Solid State Communications. 2012;152(15):1331-40.
[18] Goyal V, Balandin AA. *Thermal properties of the hybrid graphene-metal nano-micro-composites: Applications in thermal interface materials.* Applied Physics Letters. 2012;100(7):073113.
[19] Meng C, Liu C, Fan S. *A promising approach to enhanced thermoelectric properties using carbon nanotube networks.* Advanced materials. 2010;22(4):535-9.
[20] Kim KT, Choi SY, Shin EH, Moon KS, Koo HY, Lee G-G, et al. *The influence of CNTs on the thermoelectric properties of a CNT/Bi 2 Te 3 composite.* Carbon. 2013;52:541-9.
[21] Yuan W, Zhang Y, Cheng L, Wu H, Zheng L, Zhao D. *The applications of carbon nanotubes and graphene in advanced rechargeable lithium batteries.* Journal of Materials Chemistry A. 2016;4(23):8932-51.
[22] Montazeri A, Javadpour J, Khavandi A, Tcharkhtchi A, Mohajeri A. *Mechanical properties of multi-walled carbon nanotube/epoxy composites.* Materials & Design. 2010;31(9):4202-8.
[23] Wang Q, Dai J, Li W, Wei Z, Jiang J. *The effects of CNT alignment on electrical conductivity and mechanical properties of SWNT/epoxy nanocomposites*. Composites science and technology. 2008;68(7):1644-8.
[24] Kim JA, Seong DG, Kang TJ, Youn JR. *Effects of surface modification on rheological and mechanical properties of CNT/epoxy composites.* Carbon. 2006;44(10):1898-905.
[25] Zhao X, Zhang Q, Chen D, Lu P. *Enhanced mechanical properties of graphene-based poly (vinyl alcohol) composites.* Macromolecules. 2010;43(5):2357-63.
[26] Song YS, Youn JR. *Influence of dispersion states of carbon nanotubes on physical properties of epoxy nanocomposites.* Carbon. 2005;43(7):1378-85.
[27] Gojny FH, Wichmann MH, Fiedler B, Kinloch IA, Bauhofer W, Windle AH, et al. *Evaluation and identification of electrical and thermal conduction mechanisms in carbon nanotube/epoxy composites.* Polymer. 2006;47(6):2036-45.
[28] Bryning M, Milkie D, Islam M, Kikkawa J, Yodh A. *Thermal*

conductivity and interfacial resistance in single-wall carbon nanotube epoxy composites. Applied Physics Letters. 2005;87(16):161909.
[29] Yu A, Itkis ME, Bekyarova E, Haddon RC. *Effect of single-walled carbon nanotube purity on the thermal conductivity of carbon nanotube-based composites.* Applied Physics Letters. 2006;89(13):133102.
[30] Rayleigh L. LVI. *On the influence of obstacles arranged in rectangular order upon the properties of a medium.* The London, Edinburgh, and Dublin Philosophical Magazine and Journal of Science. 1892;34(211):481-502.
[31] Maxwell JC. *A treatise on electricity and magnetism:* Clarendon press; 1881.
[32] Hasselman D, Johnson LF. *Effective thermal conductivity of composites with interfacial thermal barrier resistance.* Journal of Composite Materials. 1987;21(6):508-15.
[33] Tavangar R, Molina JM, Weber L. *Assessing predictive schemes for thermal conductivity against diamond-reinforced silver matrix composites at intermediate phase contrast.* Scripta Materialia. 2007;56(5):357-60.
[34] Marconnet AM, Yamamoto N, Panzer MA, Wardle BL, Goodson KE. T*hermal conduction in aligned carbon nanotube-polymer nanocomposites with high packing density.* ACS nano. 2011;5(6):4818-25.
[35] Stauffer D, Aharony A. *Introduction to percolation theory:* CRC press; 1994.
[36] Devpura PEP, Ravi S. Prasher, Amit. *Size effects on the thermal conductivity of polymers laden with highly conductive filler particles.* Microscale Thermophysical Engineering. 2001;5(3):177-89.
[37] Hong W-T, Tai N-H. *Investigations on the thermal conductivity of composites reinforced with carbon nanotubes.* Diamond and Related Materials. 2008;17(7):1577-81.
[38] Kapitza P. *Heat transfer and superfluidity of helium II.* Physical Review. 1941;60(4):354.
[39] Jiajun W, Xiao-Su Y. *Effects of interfacial thermal barrier resistance and particle shape and size on the thermal conductivity of AlN/PI composites.* Composites Science and Technology. 2004;64(10):1623-8.
[40] Nan C-W, Liu G, Lin Y, Li M. *Interface effect on thermal conductivity of carbon nanotube composites.* Applied Physics Letters. 2004;85(16):3549-51.
[41] Helms H, Lambrecht U, Höpfner U. *Energy savings by lightweighting.* IFEU Institute for Energy-and Environmental

Research. 2003.
[42] Kang SK, Purushothaman S. *Development of conducting adhesive materials for microelectronic applications.* Journal of electronic materials. 1999;28(11):1314-8.
[43] Mirmira S, Marotta E, Fletcher L. *Thermal contact conductance of adhesives for microelectronic systems.* Journal of thermophysics and heat transfer. 1997;11(2):141-5.
[44] Fu JF, Shi LY, Zhong QD, Chen Y, Chen LY. *Thermally conductive and electrically insulative nanocomposites based on hyperbranched epoxy and nano Al2O3 particles modified epoxy resin.* Polymers for Advanced Technologies. 2011;22(6):1032-41.

Chapter 2. Synergistic Improvement of Thermal Conductivity of Thermoplastic Composites with Mixed Boron nitride and MWCNT Fillers

2.1. Introduction

Thermally conductive polymer composites are recently required for various industrial applications including heat exchangers, electronic appliances and machinery, circuit boards in power electronics [1, 2]. There is a strong interest to improve thermal conductivity of polymer composites by using carbon nanotubes (CNTs). Thermal conductivity of the CNTs along the longitudinal direction was reported as 2,800–6,000W/m·K for a single nanotube at room temperature as shown in Table 2.1. [3–10]. It is higher than graphite, carbon fibers, and even diamond [11]. The high thermal conductivity makes the CNT one of the most promising candidates of nano-fillers for thermally conductive polymer composites. However, experimentally reported thermal conductivity of the polymer/CNT composite is relatively low compared with the thermal conductivity expected by the simple rule of mixture [5, 12–15]. The low thermal conductivity is mainly caused by the high contact resistance and high interfacial thermal resistance between the CNTs and surrounding polymer matrix. The phonon transfer between CNTs was disturbed by the contact resistance and the interfacial thermal resistance hinders the phonon transfer between the CNTs and polymer matrix [16–18]. Thermally conductive polymer composites have been prepared traditionally by adding thermally conductive fillers, *e.g.*, graphite, carbon fibers, carbon blacks, ceramics or metallic particles [6–10]. Since filler volume fraction higher than 30% is usually needed to obtain thermally conductive polymer composites, which causes a significant processing challenge [19], thermally conductive polymer composites which are pelletizable and injection moldable should be

fabricated based on the thermoplastic polymer matrix. Ceramic powder filled polymer composites have been used extensively for various electronic applications. Ceramic materials such as boron nitride (BN), aluminum nitride, silicon carbide, and beryllium oxide drew more attention as thermally conductive fillers due to their high thermal and low electrical conductivities while metallic particles have high thermal and electrical conductivities [20,21].

BN particles are the most promising thermally conductive ceramic fillers because thermal conductivity of the BN particle is the highest among the ceramic materials listed in Table 2.1. CNT is also one of the promising thermally conductive fillers and suitable as the secondary filler because of the outstanding aspect ratio and intrinsic thermal conductivity. Polyphenylene sulfide (PPS) is suitable as the thermoplastic polymer matrix for thermally conductive polymer composites due to its high mechanical and thermal resistant properties [22].

In this study, PPS/BN composites were prepared with various BN weight fractions in order to develop pelletizable, injection moldable, and thermally conductive composites with low electrical conductivity and high mechanical properties. PPS/BN/multi-wall carbon nanotube (MWCNT) composites were also prepared by adding small amount of MWCNT and optimum amount of BN fillers in order to improve thermal conductivity of the composite and examine the synergistic effect on thermal conductivity of the composite [23]. Effects of the MWCNT surface treatments on thermal conductivity of the composites were investigated by modifying the MWCNT surface by peroxide and acid treatments [24] and the results were explained in terms of functionality and defect generation of the modified MWCNTs as well as interfacial thermal resistance between BN and PPS matrix. The interfacial thermal resistances of the MWCNT incorporated composites were numerically calculated by using finite element method, thereby demonstrating the influence of surface functional group on the MWCNT in enhancing the thermal conductivity of composites.

Table 2.1. Thermal conductivities of some thermally conductive fillers

Material		Thermal conductivity at 25°C(W/m·K)
Carbon	Carbon nanotubes	2800~6000
	Diamond	2000
	Graphite	100~400 (on plane)
	Pitch-based carbon fiber	530~1100 (along the axis)
	PAN-based carbon fiber	8~70 (along the axis)
	Carbon black	6~174
Ceramic	Boron nitride	250~300
	Beryllium oxide	260
	Aluminum nitride	200
	Aluminum oxide	20~29
Metal	Copper	483
	Silver	450
	Gold	345
	Aluminum	204
	Nickel	158

2.2. Experimental

2.2.1. Materials

PPS (No. E1880, Toray Resin Co., Troy, MI, U.S.A.) resin was initially supplied as powders. Average particle size of the BN powder (BORONEIGE #601, ESK Ceramics GMBH & Co., Kempten, Germany) was 3 μm and particle size distribution was ranged from 0.5 to 30 μm as shown in Fig. 2.1a MWCNT (Carbon Nano-materials Technology, Pohang, Korea) produced by the catalytic chemical vapor deposition method has the diameter of 20–100 nm, the length longer than 10 μm, and therefore the aspect ratio is larger than one hundred as shown in Fig. 2.1b.

2.2.2. Chemical Modification of MWCNT

Hydrogen peroxide and acid treatments were used to modify the MWCNT surface because these treatments have the advantage of mass production when MWCNT composites are needed. Hydrogen peroxide treatment was carried out as follows. MWCNTs was dispersed in the 1:1 mixture of H_2O_2/distilled water. Then, the mixture was sonicated for 1 h at 80 ^oC to generate carboxyl and hydroxyl groups onto the surface of MWCNTs. After the hydrogen peroxide treatment, the mixture was cleaned several times with distilled water and filtered by using a paper with pore size of 1 μm. Hydrogen peroxide treated MWCNTs was dried at 50 ^oC in a vacuum oven for 2 days. Acid treatment was also performed. Firstly, MWCNTs was dispersed in a 65 vol% solution of 3:1 volume mixture of H_2SO_4/HNO_3 in distilled water. Then, the suspension was treated by ultrasonic excitation for 1 h at 80 ^oC to attach carboxyl and hydroxyl groups onto the surface of MWCNTs. After the acid treatment, MWCNTs was cleaned several times with distilled water, filtered by using filtering paper with pore size of 1 μm, and then dried at 50 ^oC in a vacuum oven for 2 days [24].

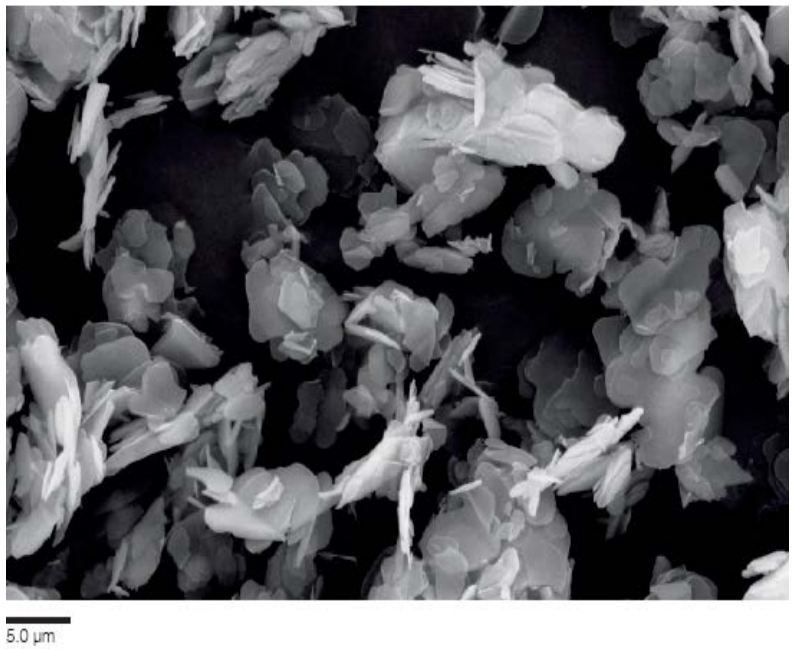

(a)

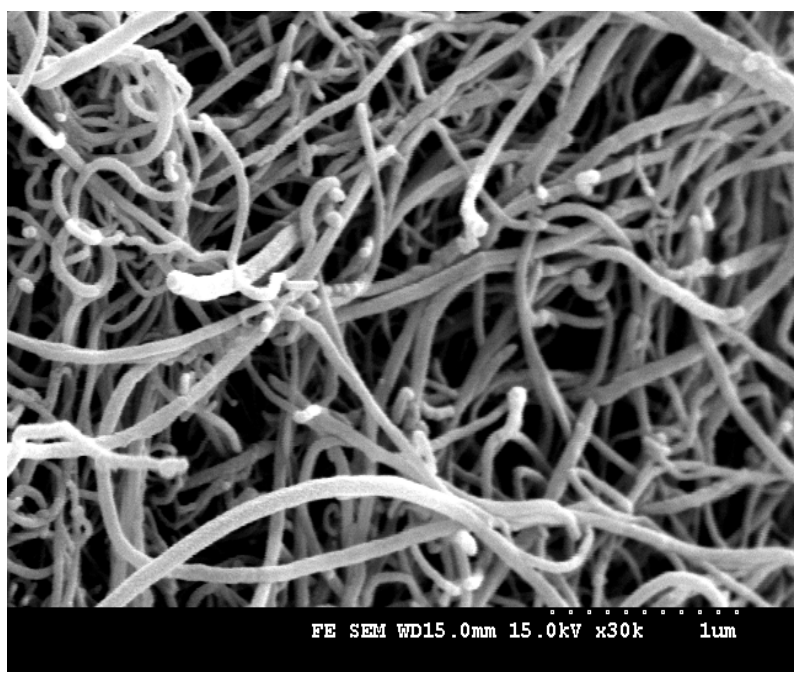

(b)

Figure 2.1 FE-SEM images of the used (a) BN powder and (b) MWCNT.

2.2.3. Surface Characterization of MWCNT

Field-emission scanning electron microscopy (FE-SEM) was employed to observe surface morphology of as-received and surface treated MWCNTs. Each sample was observed by an FE-SEM (SUPRA 55VP, Carl Zeiss Inc., Jena, Germany). As shown in Fig. 2.2., the hydrogen peroxide and acid treatments were uniformly carried out without significant reduction of length of the MWCNTs or reducing of diameter of the MWCNTs.

Raman spectroscopy analysis was performed in order to investigate surface defect of the as-received, hydrogen peroxide and acid treated MWCNTs by using a Raman spectrometer (Renishaw Raman system 2000, Renishaw Inc., IL, USA) equipped with an integral microscope (Olympus BH2-UMA, Olympus Co., NY, USA). The 632.8 nm radiation from a 17mWair cooled He/Ne laser (Model 127, Spectra Physics, Irvin, CA, U.S.A.) was used as an excitation source. Raman scattering was detected with 180o geometry using a Peltier cooled CCD detector.

Fourier transform infrared attenuated total reflection spectroscopy (FT-IR-ATR, Nicolet 6700, Thermo Scientific, Epsom, UK) was utilized in order to detect a change of functional groups created on the surface of the MWCNTs with ZnSe window. The IR spectra were obtained at the wave number range of 500–4000 cm^{-1} at a resolution of 8 cm^{-1}.

X-ray photoelectron spectroscopy (XPS, AXIS-HSi, Kratos, Kyoto, Japan) was used to determine chemical composition on the surface of the MWCNTs. The analysis was carried out with the Mg X-ray source at the power of 150W and under the pressure of 1 x 10 Torr.

2.2.4. Preparation and Characterization of Composites

Various PPS composites were prepared with various BN and MWCNT weight fractions by melt compounding using a twin-screw extruder (TEK20, SM PLATEK Co., Ansan, Korea) with a weight

feeder and the compositions of composites are listed in Table 2.2. The barrel temperature was controlled at 150, 300, 300, 290, 300, and 310 ^{o}C from the head to the die. The screw speed of 600 rpm and feeding speed of 30 rpm were maintained. The composite melt was quenched in a water bath and then pelletized using a cutting machine. Before melt compounding, the PPS resin, BN, and MWCNT powders were dried in an oven for 5 h at 100 ^{o}C to avoid void formation and degradation induced by moisture. Stair shape specimens were prepared by injection molding with an injection molding machine (HPMMC Co., Ltd., South Gyeongsang, Korea) to measure the thermal conductivity. The first set of injection molding conditions was as follows. Melt temperature was 290, 290, 290, 280, 290, and 300 ^{o}C from the cylinder to the nozzle. Injection pressure of 85 kg/cm^2, packing pressure of 35 kg/cm^2, packing time of 1 s, and mold temperature of 20 ^{o}C were applied. Higher melt temperature condition of 300, 310, 310, 300, 310 and 320 ^{o}C from the cylinder to the nozzle was applied as the second set of injection molding conditions in order to improve flowability of the molten composite. Other conditions were maintained as the same as the first set of injection molding conditions.

Morphological properties were observed with a scanning electron microscopy (SEM, JSM-6390LV, JEOL, Tokyo, Japan) to investigate dispersion of reinforcing fillers in the composite pellets. Fractured surfaces of the pellets were coated with platinum in vacuum for 80 s by using a sputter coating machine (Sputter Coater-108, Cressington Scientific Instruments, Watford, UK) and then SEM observation was carried out at 25.0 kV.

Thermal conductivity of the composite was measured with a thermal analyzer (C-Therm TCi, C-Therm Technologies Ltd., New Brunswick, Canada), which is based upon a modified transient plane source method. A known current was applied to the sensor’s heating element providing a small amount of heat. The heat provided results in a rise in temperature at the interface between the sensor and the composites, typically less than 2 ^{o}C. This temperature rises at the

interface induced a change in the voltage drop of the sensor element. The rate of increase in the sensor voltage was used to determine the thermal conductivity of the composite materials. The test was conducted at 25 ^{o}C.

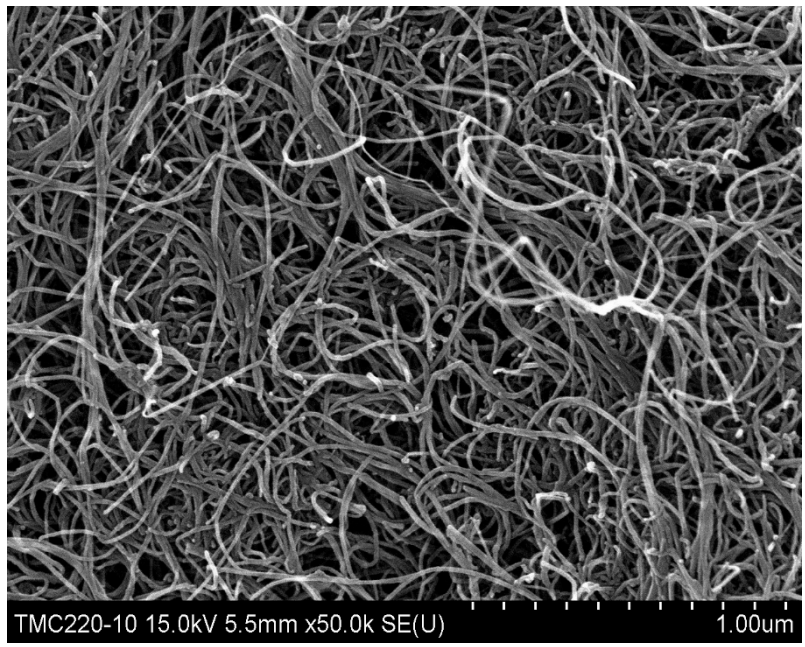

(a)

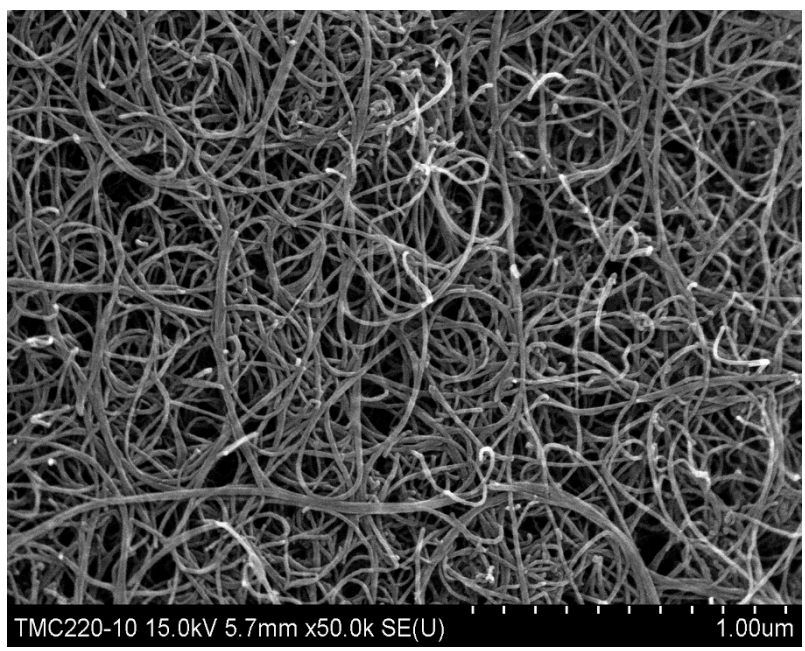

(b)

Figure 2.2 FE-SEM images of the (a) hydrogen peroxide and (b) acid treated MWCNT. Length and diameter of the MWCNT were not changed significantly after those surface treatments.

Table 2.2. Composition and thermal conductivity of the prepared materials.

Sample	PPS (wt%)	BN (wt%)	MWCNT (wt%)	Thermal Conductivity (W/m·K)
PB-0	100	0	0	0.31
PB-30	70	30	0	0.62
PB-40	60	40	0	0.87
PB-50	50	50	0	1.00
PBM-501	49	50	1	1.45
PBHM-501	49	50	1 (H_2O_2 treated)	1.74
PBAM-501	49	50	1 (acid treated)	1.31

2.3. Numerical Analysis

2.3.1. Representative Volume Element (RVE)

Fig. 2.3a displays a schematic representation of a 3D-representative volume element (3D-RVE) modelling used for investigating the effective thermal conductivity of BN-reinforced PPS composites. It was assumed that the BN particle is disc-shape plate as shown in Fig. 2.3b. According to the average length and aspect ratio of a BN from supplier data, the diameter and thickness of BN model were assigned as 3,000 nm and 200 nm. The BN volume fraction of PPS/BN composite was ranged from 20.38 to 37.4; the number of BN model was varied from 20 to 37. The RVE have the cubic geometry (L_{RVE}×L_{RVE}×L_{RVE}) and the length of cubic was calculated by following equation.

$$20.38 = \frac{V_f}{V_{RVE}} \times 100 = \frac{20 \times r^2\pi \times t}{L_{RVE}^3} \times 100, \quad (2.1)$$

It was assumed that BN particles were randomly dispersed in PPS matrix without superposition and oriented in random direction. The random number generator was used to determine the position and orientation of BN models and a BN model was not designated to intersect another BN model. Periodic boundary condition was applied to every surface of the RVE, because the composite is considered as a periodic repetition of the RVE (in other words, Unit Cell) [25]. In order to investigate the effective thermal conductivity of PPS/BN RVE, the finite element analysis was carried out by using COMSOL software.

The governing equation was applied to solve heat transfer through the RVE only considering heat conduction.

$$\rho C_p \frac{\partial T}{\partial t} = \nabla \cdot (k \nabla T) + Q, \quad (2.2)$$

where ρ is the density, C_p is the specific heat capacity, k is the thermal conductivity, and Q is the external heat change from environment to composite body. The heat transfer in the RVE is

governed by the stationary heat transfer equation and it was also assumed that there is no heat accumulation in the RVE [26]. Considering these two assumptions, following Laplace equation was applied to RVE body.

$$\nabla\left(k_{pps}\nabla\tau\right) = 0, \tag{2.3}$$

$$\nabla(k_{BN}\nabla\sigma) = 0, \tag{2.4}$$

where k_{pps} is the thermal conductivity of the PPS matrix and k_{BN} is the thermal conductivity of the BN particles, τ and σ is the unknown temperature of the PPS matrix and the BN fillers, respectively. In order to solve the Laplace equation, two boundary conditions were imposed.

1. The heat flow is defined as a constant value.
2. The other planes are set as adiabatic condition except for the planes along the heat flow direction.

In the heat conduction problem of x-direction thermal conductivity, the temperature at the nodes along the boundary $x = 0$ and $x = L_{RVE}$ are assigned as T_{hot} and T_{cold}, and temperature difference between opposite faces were designated as 1 K. In the case of adiabatic faces, following equation was applied.

$$-k_{pps}\frac{\partial\tau}{\partial\tilde{n}} = 0, -k_{BN}\frac{\partial\sigma}{\partial\tilde{n}} = 0, \tag{2.5}$$

where $\tilde{n}$ is the normal unit vector. The temperature of RVE is not continuous at the interface of the PPS matrix and the BN filler, the following equations were implied to every interface layers.

$$k_{pps}\frac{\partial\tau}{\partial\tilde{n}} = \frac{(\sigma-\tau)}{r_b}, at\ matrix\ \cap filler, \tag{2.6}$$

$$-k_{BN}\frac{\partial\sigma}{\partial\tilde{n}} = \frac{(\tau-\sigma)}{r_b}, at\ filler\ \cap matrix, \tag{2.7}$$

where r_b is the interfacial thermal resistance between the PPS matrix and the BN filler. The expression of the total heat flux along to the x direction of the RVE body is given by the following equation.

$$Q_x = K_{eff}\Delta\mathrm{T} \times \frac{L_{RVE}^2}{L_{RVE}} = -k_{PPS} \int_{A,PPS} \frac{\partial T}{\partial x} dydz - k_{BN} \int_{A,BN} \frac{\partial T}{\partial x} dydz, \quad (2.8)$$

where $\mathrm{A,PPS}$ and $\mathrm{A,BN}$ is the area of the PPS matrix and the BN filler on the planes of the RVE body along to the heat flow direction, respectively. The effective thermal conductivity of the RVE through the x-direction was calculated by using following equation

$$k_{eff,x} = -\frac{Q_x}{A_{RVE}} \frac{L_{RVE}}{(T_{cold} - T_{hot})} = \frac{Q_x}{L_{RVE}\Delta T,} \quad (2.9)$$

For the isotropic models, the thermal conductivity tensor $\boldsymbol{k}^*$ can be expressed as $\boldsymbol{k}^* = k^*\boldsymbol{I}$, where k^* is the conductivity coefficient and $\boldsymbol{I}$ is the unit tensor. Thus, the following equation was given for calculation of effective thermal conductivity of 3D-RVE.

$$k^* = \frac{\|\boldsymbol{k}^*\|}{\|\Delta T^*\|,} \quad (2.10)$$

where, ΔT^* is the temperature gradient tensor of the RVE [27]. And $\Delta\mathrm{T} = 1\ \mathrm{K}$ was induced to the all directions in this study.

2.3.2. Analytical Models

Numerous analytical models have been proposed in the literature regarding the thermal conductivity of filler reinforced composites as a function of filler content. Various analytical models have been tried to predict the thermal conductivity of heterogenic composites. Since a lot of analytical models that have been proposed are too numerous to compare with experimental results, only three models that are widely used and theoretically important are considered in present study. Maxwell model is the general theoretical model to predict the effective conductivity of heterogenic medium [28]. It was assumed that homogenous sphere particles were randomly distributed in the homogenous medium and a sphere particle is not interacted with other particles. Maxwell´s expression is given by following equation.

$$k_{eff} = k_m\left(\frac{k_f(1+2v_f) - k_m(2v_f-2)}{k_m(v_f+2) + k_f(1-v_f)}\right), \quad (2.11)$$

where k_m is the thermal conductivity of the matrix, k_f is the thermal conductivity of the filler and v_f is the volume fraction of the filler. Maxwell model is quietly well fitted with the effective thermal conductivity of the experimental results in a case of low filler vol% composite. For the high filler concentration, this model is unable to predict the effective thermal conductivity of heterogenic composite. Moreover, the shape of the filler is also not considered in this model. Hamilton proposed an analytical model which considers the shape of the filler [29]. The following equation is the expression of Hamilton model.

$$k_{eff} = k_m\left(\frac{k_f + (n-1)k_m - (n-1)v_f(k_f - k_m)}{k_f + (n-1)k_m - v_f(k_f - k_m)}\right), \quad (2.12)$$

where n is the particle shape factor related to particle sphericity Ψ with $n = 3/\Psi$. Sphericity is defined as the spherical shape of the particles and the expression of the calculation for the sphericity of the particle is given by following equations.

$$\Psi = \frac{A_s}{A_p} = \frac{\pi^{\frac{1}{3}}(6V_p)^{\frac{2}{3}}}{A_p}, \quad (2.13)$$

where A_s is the surface area of the sphere of the same volume of the particle, A_p is the surface area of the particle and V_p is the volume of the particle. Assuming the particle is spherical, Ψ equals to 1 and the value of n is 3. According to the physical property of the BN fillers which is used in this study, the value of Ψ corresponds to the 0.25. However, there are some limitations are involved; size of particle and interfacial interaction between the matrix and the particle are not considered in this model. Hamilton-Hasselman model, a coupling of Hamilton model and Hasselman model, takes into account not only size and shape factor of the particle but also interfacial thermal resistance between the particle and the matrix [30].

$$k_{eff} = k_m\left(\frac{k_f(1+(n-1)\alpha) + (n-1)k_m - (n-1)v_f\{(k_f(1-\alpha) - k_m)\}}{k_f(1+(n-1)\alpha) + (n-1)k_m - v_f(k_f(1-\alpha) - k_m)}\right), \quad (2.14)$$

where $\alpha = a_k/a_{BN}$ is the dimensionless parameter, a_k is the Kapitza radius and a_{BN} is the average radius of the BN fillers. Interfacial thermal resistance r_b (also called as the Kapitza resistance) is calculated from following equation.

$$r_b = \frac{a_k}{k_m}, \tag{2.15}$$

2.3.3. Computation Details

It is hard to construct the Representative volume element of the PPS/BN/MWCNT due to extremely high aspect ratio of MWCNT. Therefore, in order to estimate the effective thermal conductivity of PPS/BN/MWCNT composite, several assumptions were required. Firstly, PPS/MWCNT was regarded as a homogeneous medium for simplifying the RVE of PPS/BN/MWCNT composite. It was also assumed that MWCNTs were randomly distributed in homogeneous medium. In this regard, thermal conductivity of matrix (PPS/MWCNT) is only depended on the volume fraction of MWCNT. Incorporation of MWCNT affects the thermal interfacial resistance between the PPS matrix and the BN fillers due to the functional groups on MWCNT surface [31]. In order to prove the effect of surface treated MWCNT, the interfacial thermal resistance of the PPS/BN/MWCNT composites were numerically calculated by using finite element analysis.

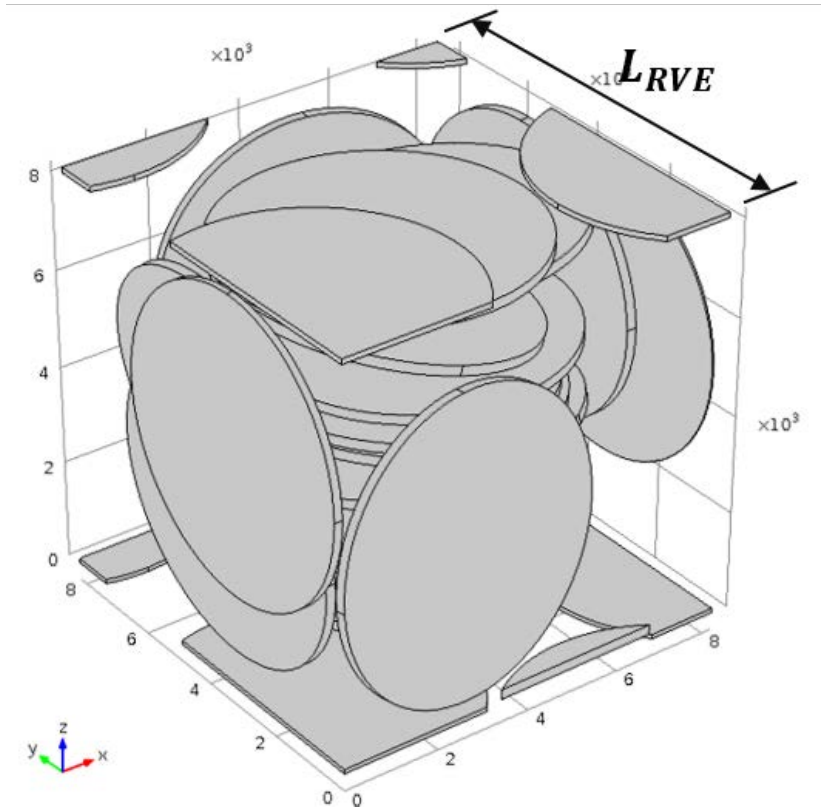

(a)

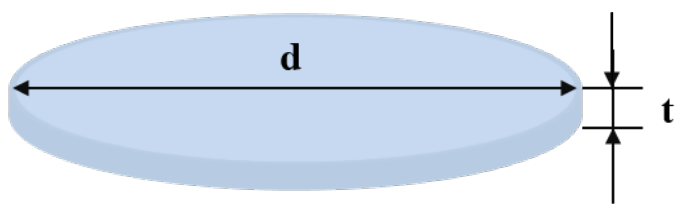

(b)

Figure 2.3. Three-dimensional geometry of (a) representative volume element and (b) BN filler.

2.4. Results & Discussion

2.4.1. Moldability of Composites

Appearance of the injection molded specimen is shown in Fig. 2.4. with respect to the BN weight fraction. The injection molded specimen was composed of three different thicknesses in order to estimate moldability of the injected material. As shown in Fig. 2.4c, the thin part of the injection molded composite specimen with BN of 50 wt% was not filled completely due to the increased viscosity of the composite with increasing BN weight fraction. Higher loading of BN fillers in the composite was not preferable because of the poor moldability of the highly filled composite material. When using the second set of injection molding conditions, all the composites listed in Table 2.2 were pelletized and injection molded due to higher melt temperature applied. Therefore, the pelletizable and injection moldable thermoplastic composites were successfully prepared and the first objective of present study was satisfied.

2.4.2. Thermal Conductivity of Composites

Thermal conductivity of the PPS/BN composites is listed in Table 2.2. with respect to BN weight fraction and the thermal conductivity of composite was enhanced with increasing BN loading, proving that BN is one of the most effective thermally conductive ceramic fillers. Teng et al. [32] recently reported synergistic effect of chemically connected BN and MWCNT on the thermal conductivity of epoxy composites. Significant improvement of thermal conductivity was observed in this study when small amount of MWCNTs was added to the thermoplastic composite by using conventional melt compounding. The synergistic effect depended on the surface treatment of MWCNTs significantly as shown in Table 2.2. These results indicated that the synergistic effect was caused by physical properties of both BN and MWCNT.

(a) (b) (c)

Fig 2.4. Appearance of the injection molded specimens with the first set of injection conditions: (a) PB-30, (b) PB-40, and (c) PB-50.

2.4.3. Morphology

Fracture surface of the PPS/BN/MWCNT composite is displayed in Fig. 2.5a. The polygon shape of the BN filler was clearly observed but the MWCNTs indicated with the red arrows was not clearly identified due to the fibril structure of PPS matrix. Surface of the PPS/BN/MWCNT composite pellet was fired with a torch for about 30 seconds in order to remove the fibril structure or texture of the PPS matrix. The MWCNTs was clearly observed at the boundary of BN fillers in the burned surface as shown in Fig. 2.5b. Aggregation of BN and MWCNT fillers shown in Fig. 2.5c was observed rarely on the pellet surface of the PPS/BN/MWCNT composite, indicating existence of spontaneous attraction between the BN and MWCNT during melt compounding. It was suggested by the results that the synergistic effect of the PPS/BN/MWCNT composites was obtained because the amount of thermally conductive fillers was increased by adding incorporated MWCNT and three-dimensional thermal transfer pathway was formed between the BN and MWCNT fillers owing to high aspect ratio of MWCNT as shown in the schematic diagram of Fig. 2.5d.

Considering the intrinsic outstanding thermal conductivity of BN and MWCNT fillers, dissatisfied improvement of the thermal conductivity of the prepared composites can be understood by the following three reasons. Firstly, perfect three dimensional networks between thermally conductive fillers cannot be constructed. Secondly, high interfacial thermal resistance between the polymer matrix and BN filler also occurred. Therefore, defect of the MWCNT related to the intrinsic thermal conductivity of the MWCNT, and functionality of the MWCNT associated with the interfacial interaction and interfacial thermal resistance between PPS matrix and BN should be investigated in order to understand dependence of the synergistic effect on the surface treatment of the MWCNT.

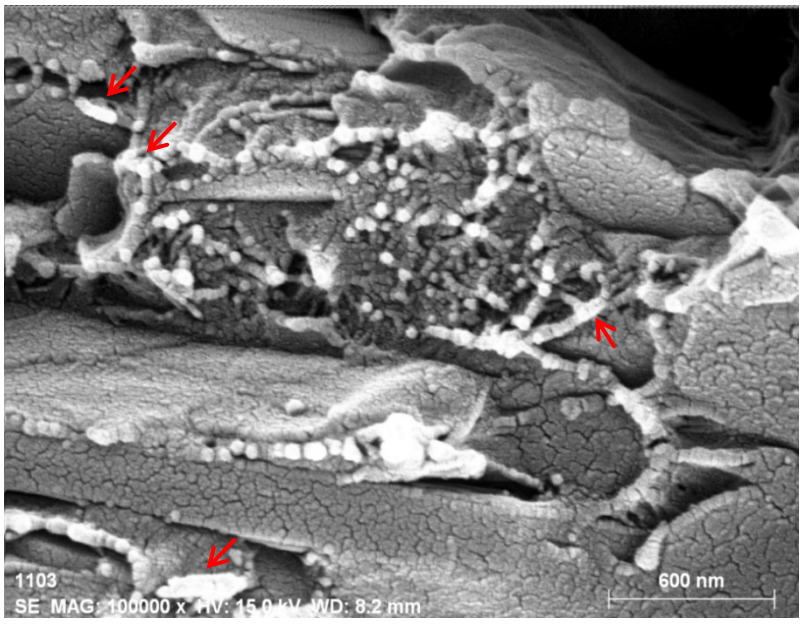

(a)

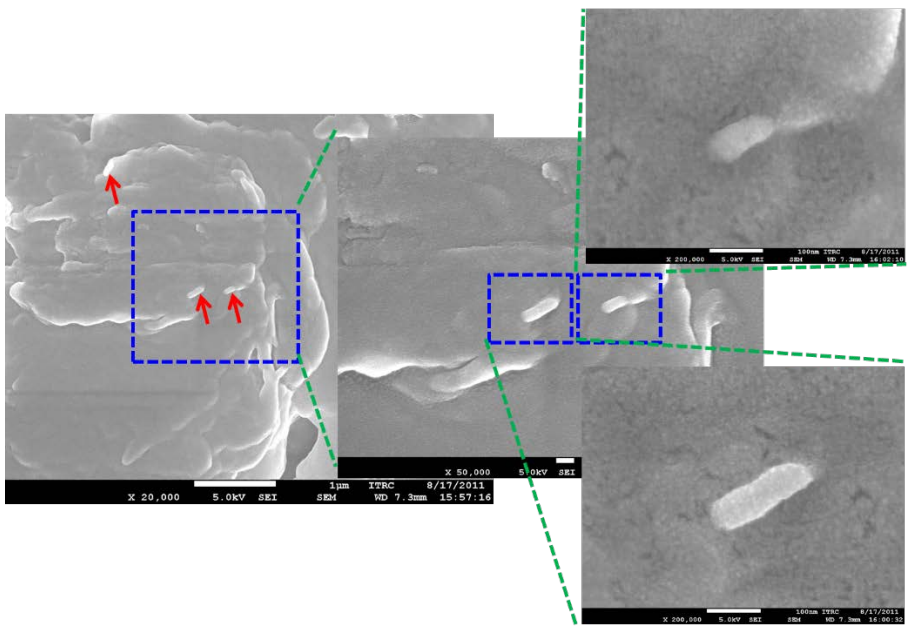

(b)

Figure 2.5. FE-SEM images of (a) fractured surface of PBM-1 composite, (b) burned surface of the PBM-1 composite, (c) aggregation of BN and MWCNT fillers rarely observed at the pellet surface of the PBM-1 and (d) schematic diagram of the BN/MWCNT filler network in the PBM composite.

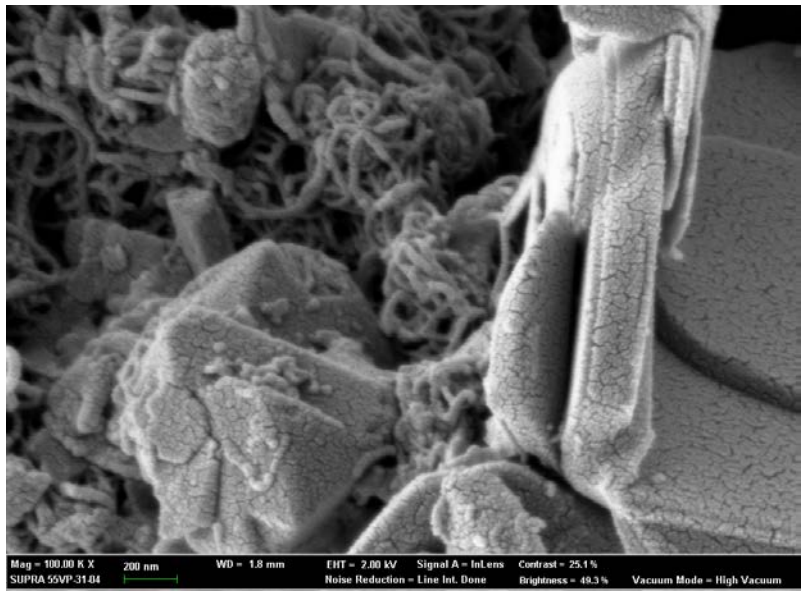

(c)

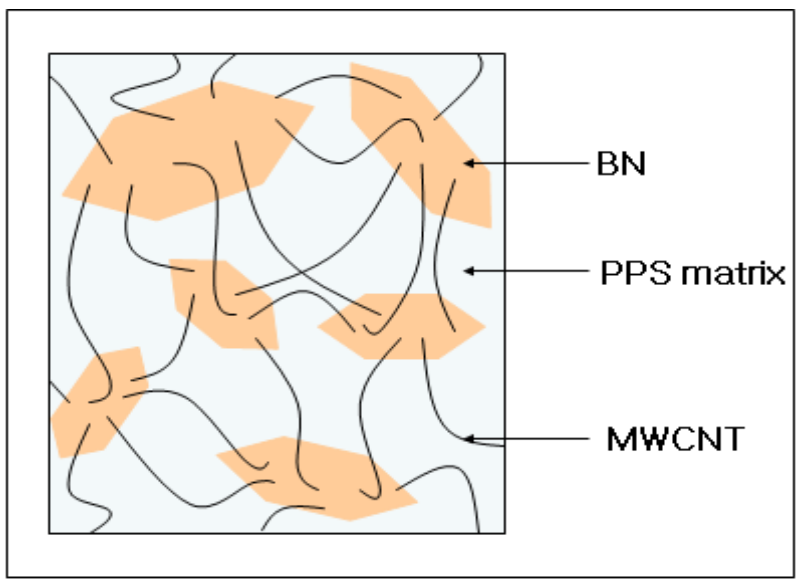

(d)

Figure 2.5. (Continued)

2.4.4. Defect and functionality of MWCNT

Raman spectroscopy is a reliable tool for characterization of the defect on MWCNT. The Raman spectra of pristine, hydrogen peroxide treated, and acid treated MWCNTs are shown in Fig. 2.6. Each spectrum consisted of three characteristic bands, namely the D-band at ~1338 cm^{-1}, the G-band at ~1572 cm^{-1} and the D´-band at ~1608 cm^{-1}. The D-band is a disorder induced feature arising from double resonance Raman scattering process from a non-zero-center phonon mode [33–36]. The D band is usually attributed to the presence of amorphous or disordered carbons. The disordered carbon structure is due to the finite or nano-sized graphitic planes and other forms of carbons, e.g., rings along with defects on the nanotube walls, vacancies, heptagon-pentagon pairs, kinks and heteroatoms. The G band originates from in-plane tangential stretching of the carbon–carbon bonds in graphene sheets. The D´ band which is a weak shoulder of the G-band at higher frequencies is also a double resonance feature induced by disorder and defects. Typically, the ratio of intensities between the D and G bands (ID/IG) of the CNT in Raman spectroscopy is taken as a measure of defects in CNT [34]. The ID/IG ratio of pristine, hydrogen peroxide treated, and acid treated MWCNT is summarized in Table 2.3. The increase of defects on the hydrogen peroxide treated MWCNT was confirmed by the upshift of the D band and the increased ID/IG ratio from 0.82 to 0.93. Introduction of defects like junctions on CNT usually gives rise to an increase of the local thermal resistance and reduces the thermal conductivity due to lattice defects [37, 38]. However, the highest thermal conductivity of the PBHM-501 composite shown in Table 2.2 implied that the defects on the hydrogen peroxide treated MWCNT had insignificant effects on the thermal conductivity and another dominant physical factor determining thermal conductivity of the composite existed.

The FT-IR spectra of the pristine, acid treated, and hydrogen peroxide treated MWCNTs are shown in Fig. 2.7a. The characteristic

bands indicating generation of functional groups were observed in the spectrum of each surface treated MWCNT. Fig. 2.7b shows the O–H peak intensity at 3432 and 1588 cm^{-1} that represents hydroxyl groups for the hydrogen peroxide treated MWCNT. In addition, the peaks at about 1060 cm^{-1} belong to oxygen groups resulting from the oxidation. They indicate that the hydroxyl groups and oxygenated groups are produced by the treatment [39]. As shown in Fig. 2.7c, newly generated peaks were obviously observed in the spectrum of the acid treated MWCNT in comparison with the spectrum of the pristine MWCNT. The peaks around 3421 and 1453 cm^{-1} were assigned to the O–H band, and the peaks at 1654 and 1710 cm^{-1} are assigned to the C=O band for carboxyl groups, demonstrating generation of hydroxyl and carboxyl groups on the MWCNT surface by the acid treatment [40,41].

Surface elemental composition of the pristine, hydrogen peroxide treated, and acid treated MWCNTs was analyzed by the XPS [42]. Each peak was fitted by using binding energy of standard carbon, 284.6 eV and the C ls XPS spectra of pristine and surface treated MWCNTs are shown in Fig. 2.8a. The asymmetric peak at 284.6 eV is assigned to sp^2-hybridized graphite-like carbon atoms and sp^2 carbon atoms bound to hydrogen and the main peaks of the pristine and surface treated MWCNTs were observed at the similar binding energy. The Gaussian peak at 285.3 eV of the pristine MWCNT shown in Fig. 2.8a is originated from sp^3-hybridized carbon atoms and is similar to that of the diamond like carbon. In Fig. 2.8b, the Gaussian peak at 285.3 eV caused by sp^3-hybridized carbon atoms of the hydrogen peroxide treated MWCNT was also observed, indicating dominant existence of diamond like carbons and alcohol groups (C–OH). The peak at 286.2 eV shown in Fig. 2.8c is a typical peak of carbon atoms bound to oxygen atoms by single bond influenced by the carboxylic acid [43].

Fig. 2.9 shows the O ls XPS spectra of the pristine and surface treated MWCNTs. Specific oxygen peaks do not exist for the pristine MWCNT as shown in Fig. 2.9a. Two peaks at 531.7 and 533.0 eV in Fig. 2.9b and 2.9c for the hydrogen peroxide treated and acid treated

MWCNTs are originated from oxygen atoms bound to carbon atoms in the functional groups like alcohol (C–OH) and carboxylic acid (COOH), respectively [43]. The alcohol peak was more apparent than the carboxylic acid peak in the case of the hydrogen peroxide treated MWCNT, implying that alcohol groups were dominantly introduced by the hydrogen peroxide treatment. The opposite result that the carboxylic acid peak was larger than alcohol peak was observed in the case of the acid treated MWCNT and the O 1s peak of the acid treated MWCNT was much larger than that of other MWCNT samples, suggesting that carboxylic acid groups were dominantly generated by the acid treatment. The results were in good agreement with those of the C 1s XPS spectra and FT-IR, and it is well known that generation of different functional groups on the surface of MWCNT can alter interfacial interaction with the polymer matrix.

Thermal conductivity of the PPS/MWCNT composite with MWCNT of 1 wt% is also listed in Table 2.2 with respect to surface treatment method of MWCNT. The MWCNT of 1 wt% was selected based on the experimental results of the reference [32]. Thermal conductivity of the PPS/MWCNT composite was increased by adding MWCNT of 1 wt% and depended on the surface treatment of MWCNT. These results demonstrated that the interfacial interaction and interfacial thermal resistance between the PPS matrix and MWCNT were varied depending upon the surface treatment of the MWCNT and the synergistic effect was observed for the composites [17,18].

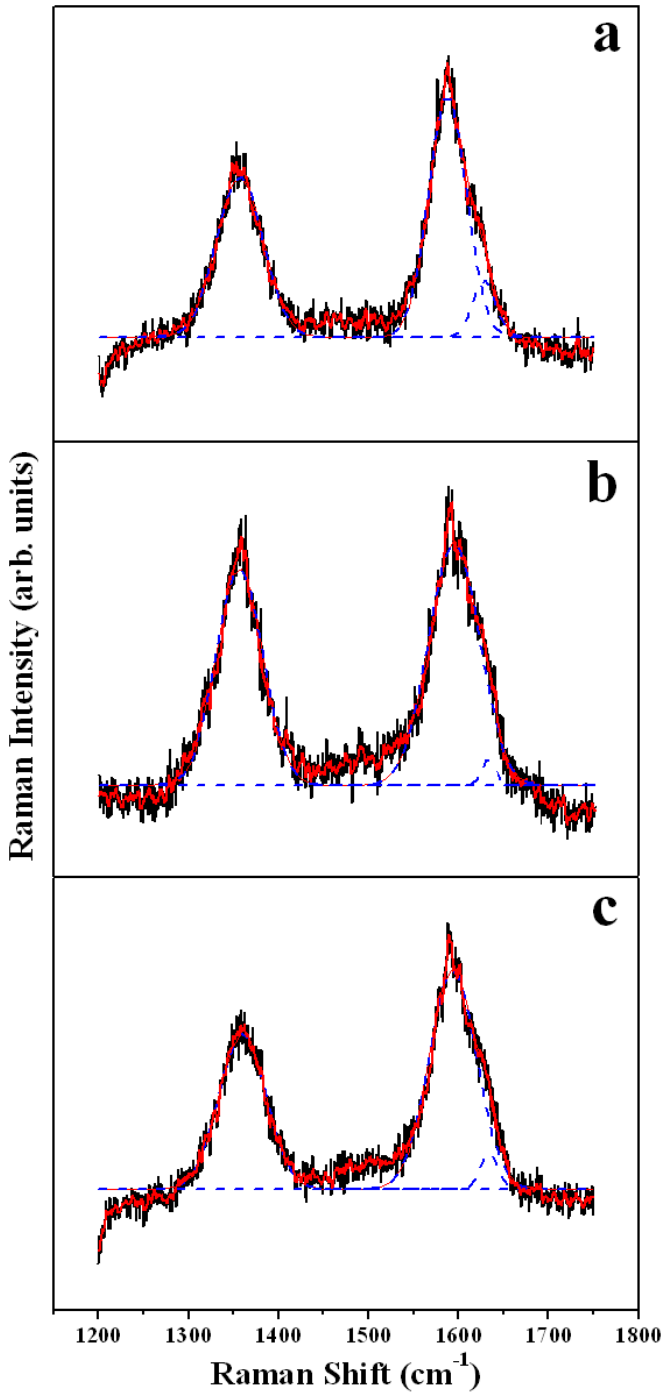

Figure 2.6. Raman spectra of (a) pristine, (b) hydrogen peroxide treated, and (c) acid treated MWCNT samples.

Table 2.3. ID/IG intensity ratio of the MWCNT samples.

	Pristine MWCNT	H2O2 treated MWCNT	Acid treated MWCNT
ID/IG	0.82	0.93	0.80

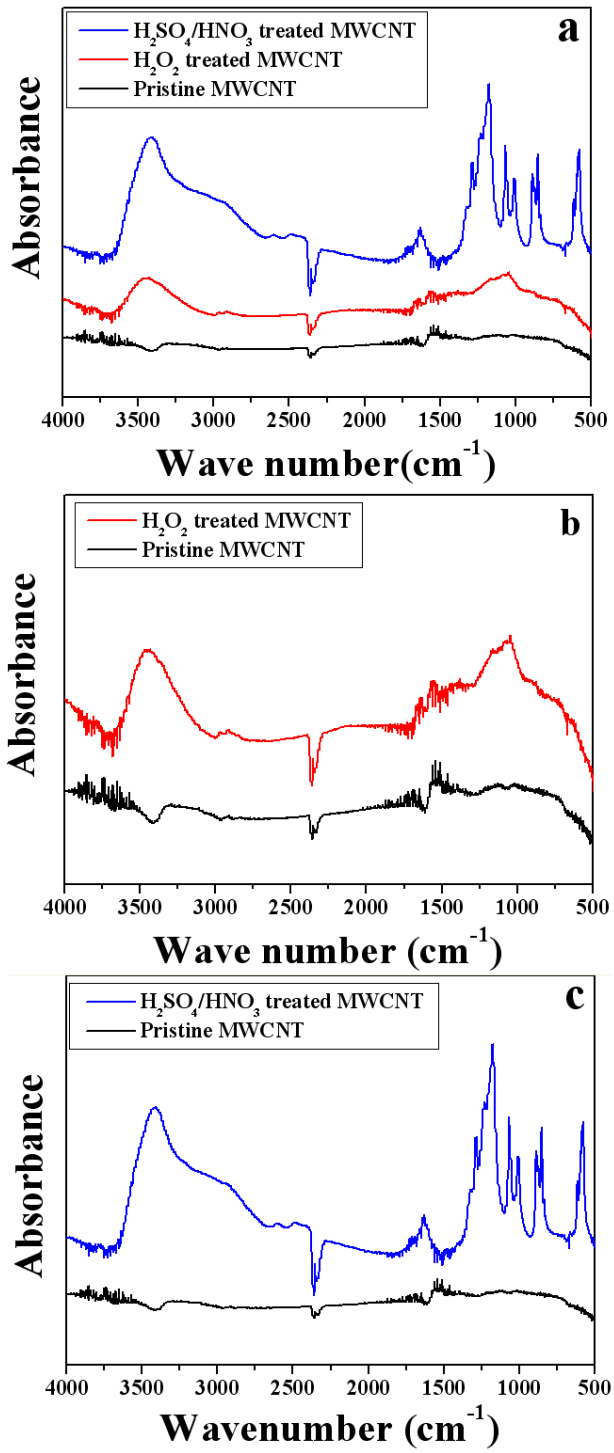

Figure 2.7. (a) FT-IR absorbance spectra of pristine, hydrogen peroxide treated, and acid treated MWCNTs, (b) comparison between pristine and hydrogen peroxide treated MWCNTs and (c) comparison between pristine and acid treated MWCNTs.

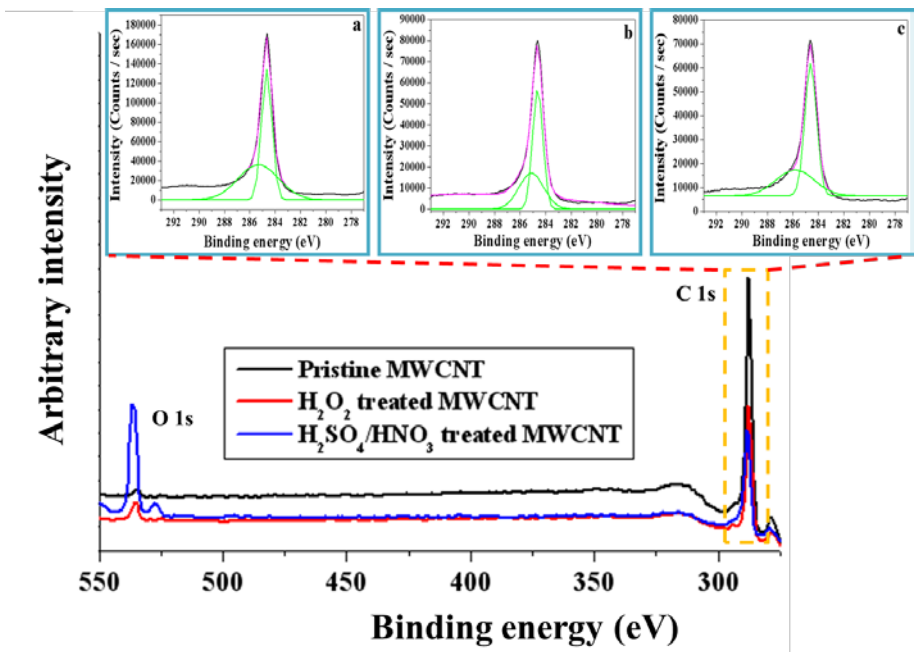

Fig. 2.8. XPS spectra of pristine, hydrogen peroxide treated, and acid treated MWCNT samples. The inserted figures are enlarged XPS spectra and Gaussian peaks for the C 1s peak of (a) pristine, (b) hydrogen peroxide treated, and (c) acid treated samples.

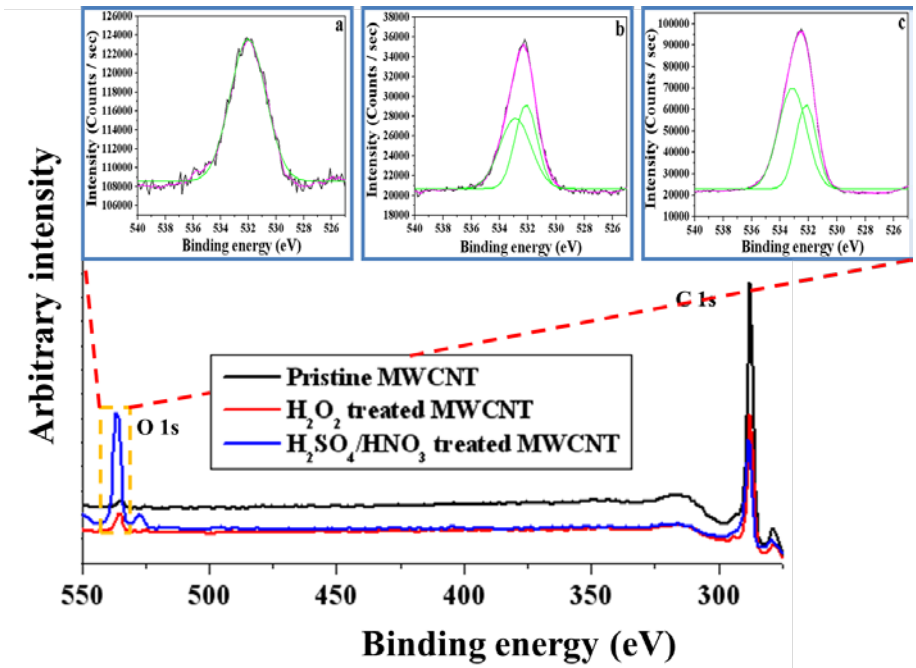

Fig. 2.9. XPS spectra of pristine, hydrogen peroxide treated, and acid treated MWCNT samples. The inserted figures are enlarged XPS spectra and Gaussian peaks for the O 1s peak of (a) pristine, (b) hydrogen peroxide treated, and (c) acid treated samples.

2.4.5. Numerical Results

The thermal conductivities of PP/BN composites obtained from experiments and analytical calculation are compared with a function of BN volume fraction as shown in Fig. 2.10. The results indicated that the experimental trends of the thermal conductivities do not fitted with the Maxwell model curve. This disagreement can be explained by the simplicity of Maxwell model which do not consider the particle-particle interaction and the geometry of the particle. The Hamilton model having low sphericity ($\Psi = 0.25$ corresponding to the BN particle used in present study) shows large discrepancy with experimental values because the Hamilton model does not take into the interaction between the matrix and the particle at the interface. However, the Hamilton-Hasselman model ($\alpha = a_k/a_{BN} = 0.13$ and $\Psi = 0.25$) is the most suited model to describe the thermal conductivity of the PPS/BN composite. The Kapitza radius a_k can be calculated from the average radius of BN and α which were obtained in this study. Considering $a_k = 308.26$ nm of PPS/BN composite, R_b = 1E-6 K·m^2/W was also calculated.

The thermal conductivity of the PPS/BN composite with respect to the interfacial thermal resistance were estimated by using COMSOL software. The simulation results shown in Fig. 2.11 implied that thermal conductivity of PPS/BN composite was strongly depended on the interfacial thermal resistance. When the interfacial resistance was ranged from 1E-5 to the 1E-8 K·m^2/W, the thermal conductivity of PPS/BN composite was dramatically changed. When the interfacial thermal resistance is higher than 1E-4 K·m^2/W, the value of thermal conductivity for 50 wt% BN loading sample became lower than that of the other samples. This result suggested that the BN acts like obstacles at the range. The thermal conductivities obtained from experiments were well fitted to numerically calculated thermal conductivities at 1E-6 K·m^2/W of the interfacial thermal resistance (See Fig. 2.11b) Based on the comparison, we set the interfacial thermal resistance as 1E-6

$K \cdot m^2/W$ for the numerical analysis. Fig. 2.12 shows the numerically calculated thermal conductivity of PPS/BN composites with respect to BN volume fraction by using finite element method. The result shows that finite element method is the most suited approach to predict the effective thermal conductivity rather than analytical models. From this investigation, the numerical simulation is useful to predict interfacial thermal resistance between the PPS and the BN.

In order to calculate the effective thermal conductivity of the PPS/BN/MWCNT composites, it is also necessary to measure the thermal conductivity of PPS/MWCNT composites. The thermal conductivities of PPS/MWCNT composites were tabulated in Table 2.4. The functionality of the MWCNT was expected to play a critical role for determining the effective thermal conductivity of composites. In other words, the interfacial thermal resistance between the PPS and the BN can be changed by surface modification of MWCNT. Fig. 2.13 revealed the interfacial thermal resistance of PPS/BN/MWCNT composites and the values are summarized in Table 2.5. The highest and lowest interfacial thermal resistance of PBAM-501 composite have accordance with the experimental results. The thermal conductivity of PBAM-501 as a function of interfacial thermal resistance is shown in Fig. 2.14. Thermal conductivity of PBAM-501 was rapidly increased with decreasing the interfacial thermal resistance in the range from 1E-6 to 1E-7 $K \cdot m^2/W$. The results implied that the thermal conductivity of PPS/BN/MWCNT composite can be enhanced by manipulating of the interfacial thermal resistance between the matrix and the filler. The specific thermal conductivity is also estimated and the highest value is comparable to the half of aluminum, allowing the PPS/BN/MWCNT to replace the metal for automotive applications.

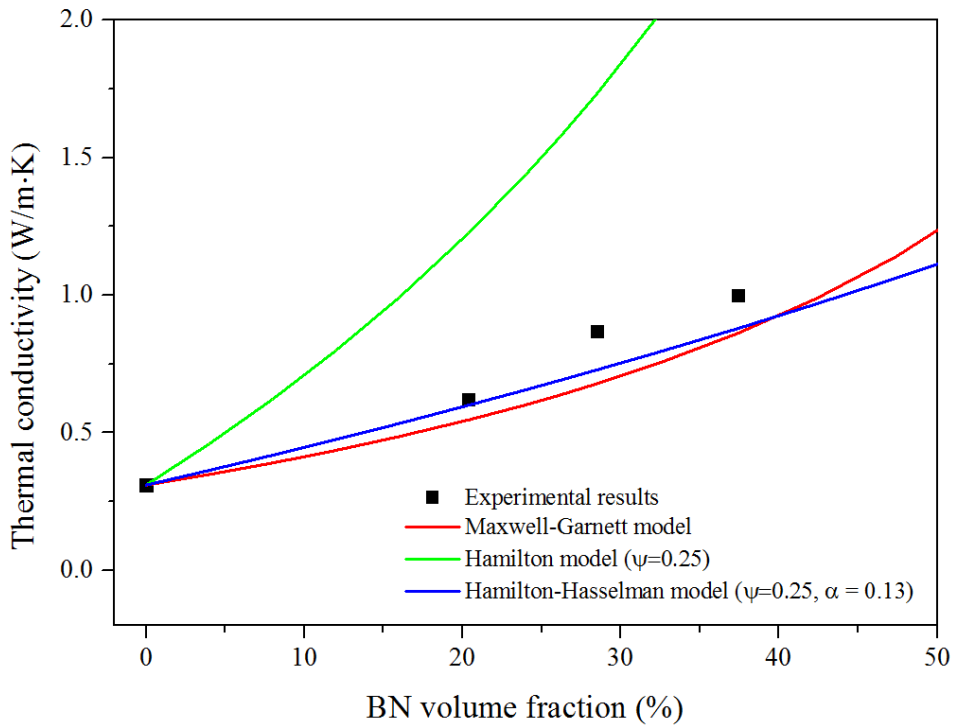

Figure 2.10. The experimental data and theoretical curve of the thermal conductivity of PPS/BN composites.

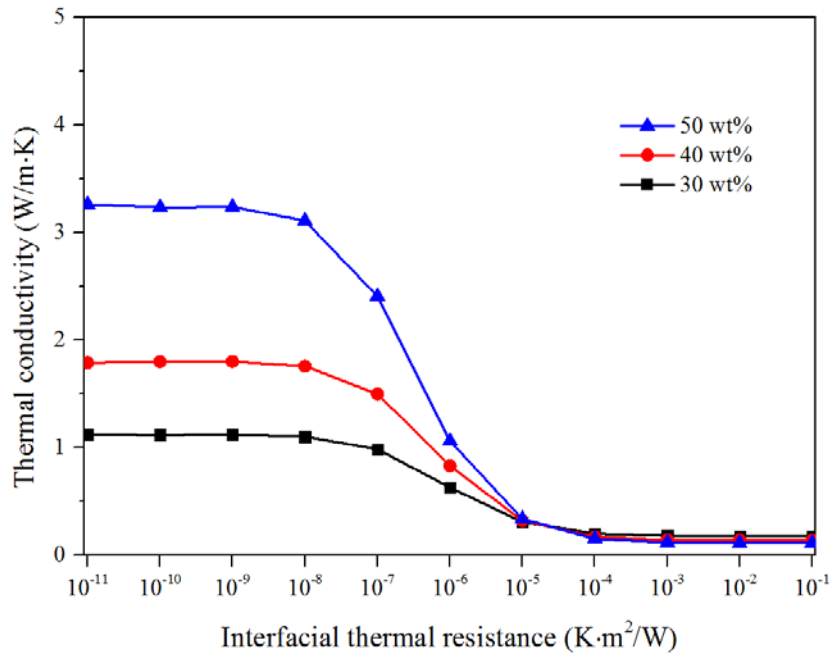

(a)

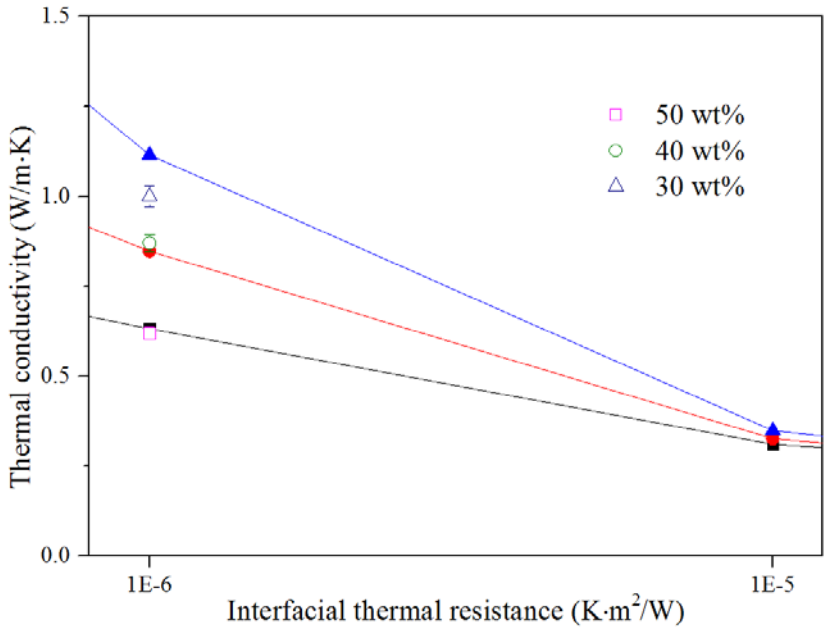

(b)

Fig. 2.11. (a) The effect of the interfacial thermal resistance on thermal conductivity of the composite and (b) comparison between the experimental data and numerical results.

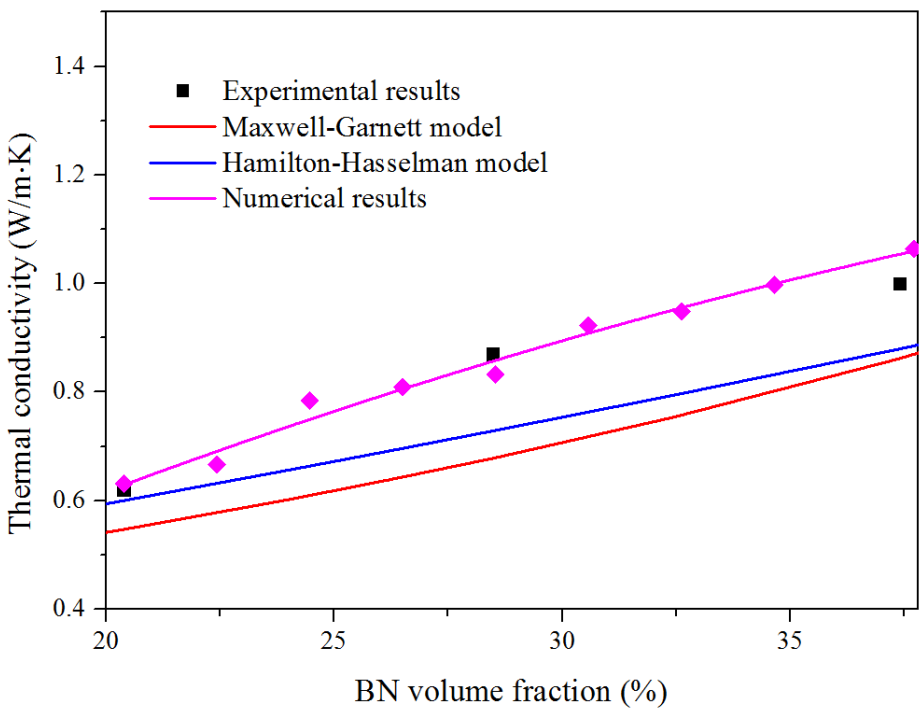

Figure 2.12. The experimental data and the numerical curves of the thermal conductivity of PPS/BN composites.

Table 2.4. Composition and thermal conductivity of the prepared PPS/MWCNT composites.

Sample	PPS (wt%)	BN (wt%)	MWCNT (wt%)	Thermal Conductivity (W/m·K)
PM-1	99	0	1	0.48
PBM-1	99	0	1 (H_2O_2 treated)	0.55
PAM-1	99	0	1 (acid treated)	0.42

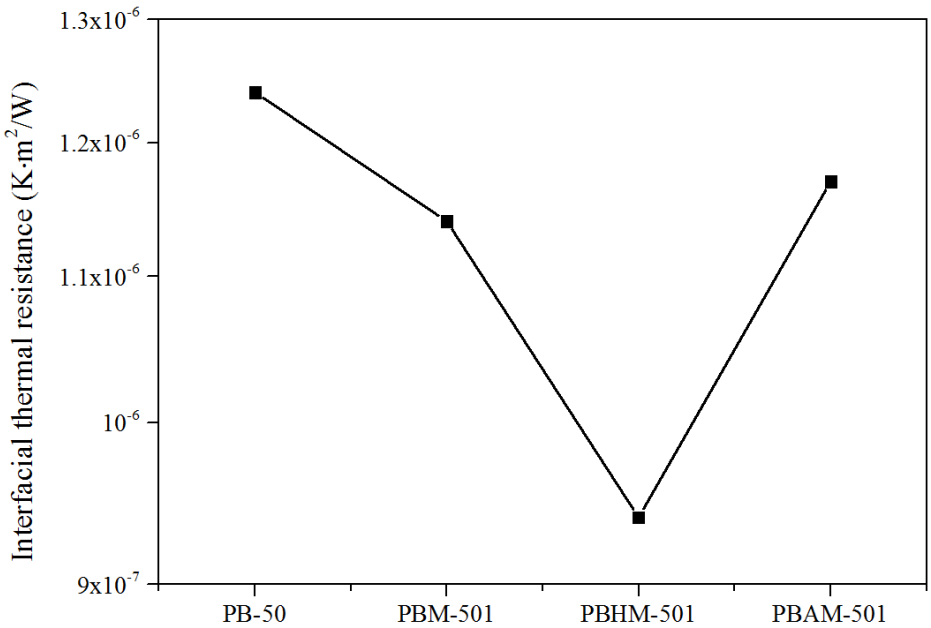

Figure 2.13. Interfacial thermal resistance of PPS/BN/MWCNT composites.

Table 2.5. Interfacial thermal resistance of PPS/BN/MWCNT composites

Sample	PPS (wt%)	BN (wt%)	MWCNT (wt%)	Interfacial thermal resistance ($K \cdot m^2/W$)
PB-50	50	50	0	1.24E-6
PBM-501	49	50	1	1.14E-6
PBHM-501	49	50	1 (H_2O_2 treated)	9.4E-7
PBAM-1	49	50	1 (acid treated)	1.17E-6

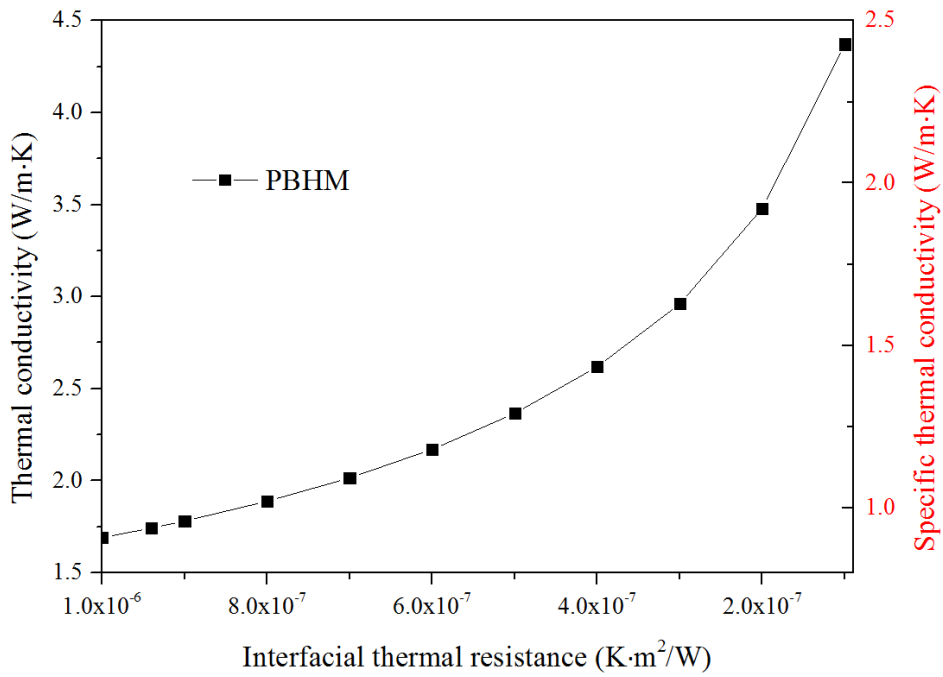

Figure 2.14. Numerically estimated thermal conductivity and specific thermal conductivity for PBAM-501 composite with decreasing interfacial thermal resistance.

2.5. Summary

Pelletizable, injection moldable, and thermally conductive thermoplastic PPS/BN composites were prepared. Thermal conductivity of the composite was improved with increasing BN loading because BN is one of the most thermally conductive ceramic fillers. PPS/BN/MWCNT composites were also prepared for further improvement of the thermal conductivity by adding both MWCNT of 1 wt% and BN fillers of 50 wt%. Synergistic improvement in the thermal conductivity of the PPS/BN/MWCNT composite was observed because the amount of thermally conductive fillers was increased by incorporating additional MWCNTs and three dimensional heat transfer pathway was generated between BN and MWCNT fillers owing to high aspect ratio of the MWCNT. The synergistic improvement in the thermal conductivity of the PPS/BN/MWCNT composite depended strongly on the surface treatment of the MWCNTs such as hydrogen peroxide and acid treatments. Hydroxyl groups were generated dominantly on the surface of the MWCNT by the hydrogen peroxide treatment and more defects were induced on the surface of the hydrogen peroxide treated MWCNT. Carboxylic groups were introduced dominantly in the case of the acid treatment. The different functionality of surface treated MWCNT affected interfacial interaction and interfacial thermal resistance between the PPS matrix and MWCNT. Therefore, the synergistic improvement depended on the surface treatment of the MWCNT and was attributed to the variation of the interfacial interaction and interfacial thermal resistance. Moreover, the effect of the interfacial thermal resistance between the PPS matrix and the BN filler were investigated quantitatively by using finite element method.

2.5. References

[1] Pernot G, Stoffel M, Savic I, Pezzoli F, Chen P, Savelli G, et al. *Precise control of thermal conductivity at the nanoscale through individual phonon-scattering barriers*. Nat Mater 2010;9:491-5.
[2] Shaikh S, Lafdi K, Silverman E. The effect of a CNT interface on the thermal resistance of contacting surfaces. Carbon 2007;45:695-703.
[3] Kim P, Shi L, Majumdar A, McEuen PL. *Thermal transport measurements of individual multi walled nanotubes*. Phys Rev Lett 2001;87:215502-1-4.
[4] Yu C, Shi L, Yao Z, Li D, Majumdar A. *Thermal conductance and thermopower of an individual single-wall carbon nanotube*. Nano Lett 2005;5:1842-6.
[5] Han Z, Fina A. *Thermal conductivity of carbon nanotubes and their polymer nanocomposites: A review*. Prog Polym Sci 2011;36:914-44.
[6] Pierson HO. *Handbook of carbon, graphite, diamond and fullerenes: properties, processing, and applications*. NJ: Noyes Publications; 1993.
[7] Wypych G. *Handbook of fillers: physical properties of fillers and filled materials.* Toronto: ChemTec Publishing; 2000.
[8] Fischer JE. *Carbon nanotubes: structure and properties.* In: Gogotsi Y, editor. Carbon nanomaterials. New York: Taylor and Francis Group; 2006. p. 51-8.
[9] Wolff S, Wang MJ. *Carbon black science & technology. 2nd* ed. New York: Marcel Dekker; 1993.
[10] Kelly BT. *Physics of graphite*. Barking (UK): Applied Science Publishers; 1981.
[11] Guthy C, Du F, Brand S, Winey KI, Fischer JE. *Thermal conductivity of SWCNT/PMMA nanocomposites*. J Heat Transfer 2007;129:1096-9.
[12] Shen Z, Bateman S, Wu DY, McMahon P, Dell' Olio M, Gotama J. *The effects of carbon nanotubes on mechanical and thermal properties of woven glass fiber reinforced polyamide-6*

nanocomposites. Compos Sci Technol 2009;69:239-44.
[13] Nan CW, Liu G, Lin Y, Li M. *Interface effect on thermal conductivity of carbon nanotube composites*. Appl Phys Lett 2004;85:3549-51.
[14] Song YS, Youn JR. *Evaluation of effective thermal conductivity for carbon nanotube/polymer composites using control volume finite element method.* Carbon 2006;44:710-7.
[15] Song YS, Youn JR. *Influence of dispersion states of carbon nanotubes on physical properties of epoxy nanocomposites*. Carbon 2005;43:1378-85.
[16] Shenogina N, Shenogin S, Xue L, Keblinski P. *On the lack of thermal percolation in carbon nanotube composites.* Appl Phys Lett 2005;87:133106-1-3.
[17] Huxtable ST, Cahill DG, Shenogin S, Xue L, Ozisik R, Barone P, et al. *Interfacial heat flow in carbon nanotube suspensions*. Nat Mater 2003;2:731-4.
[18] Shenogin S, Xue L, Ozisik R, Keblinski P, Cahill DG. *Role of thermal boundary resistance on the heat flow in carbon nanotube composites*. J Appl Phys 2004;95:8136-44.
[19] King JA, Barton RL, Hauser RA, Keith JM. *Synergistic effects of car bon fillers in electrically and thermally conductive liquid crystal polymer based resins*. Polym Compos 2008;29:421-8.
[20] Raman C, Meneghetti P. *Boron nitride finds new applications in thermoplastic compounds.* Plast Addit Compound 2008;10:26-31.
[21] Ishida H, Rimdusit S. *Very high thermal conductivity obtained by boron nitride-filled polybenzoxazine*. Thermochim Acta 1998;320:177-86.
[22] Zhao YF, Xiao M, Wang SJ, Ge XC, Meng YZ. *Preparation and properties of electrically conductive PPS/expanded graphite nanocomposites.* Compos Sci Technol 2007;67:2528-34.
[23] Yu A, Ramesh P, Sun X, Bekyarova E, Itkis ME, Haddon RC. *Enhanced thermal conductivity in a hybrid graphite nanoplatelet-carbon nanotube filler for epoxy composites*. Adv Mater 2008;20:4740-4.
[24] Lee SH, Choi SH, Kim SY, Youn JR. *Effects of thermal*

imidization on mechanical properties of poly(amide-co-imide)/multiwalled carbon nanotube composite films. J Appl Polym Sci 2010;117:3170-80.
[25] KANIT, T., et al. *Determination of the size of the representative volume element for random composites: statistical and numerical approach*. International Journal of solids and structures, 2003, 40.13: 3647-3679.
[26] MENDES, Miguel AA, et al. *Detailed and simplified models for evaluation of effective thermal conductivity of open-cell porous foams at high temperatures in presence of thermal radiation*. International Journal of Heat and Mass Transfer, 2014, 68: 612-624.
[27] MARCOS-GOMEZ, D., et al. *Predicting the thermal conductivity of composite materials with imperfect interfaces. Composites* Science and Technology, 2010, 70.16: 2276-2283.
[28] MAXWELL, James Clerk. *A treatise on electricity and magnetism. Clarendon press*, 1881.
[29] PROGELHOF, R. C.; THRONE, J. L.; RUETSCH, R. R. *Methods for predicting the thermal conductivity of composite systems: a review*. Polymer Engineering & Science, 1976, 16.9: 615-625.
[30] JIAJUN, Wang; XIAO-SU, Yi. *Effects of interfacial thermal barrier resistance and particle shape and size on the thermal conductivity of AlN/PI composites.* Composites Science and Technology, 2004, 64.10: 1623-1628.
[31] YANG, Shin-Yi, et al. *Effect of functionalized carbon nanotubes on the thermal conductivity of epoxy composites*. Carbon, 2010, 48.3: 592-603.
[32] Teng CC, Ma CCM, Chiou KC, Lee TM, Shih YF. *Synergetic effect of hybrid boron nitride and multi-walled carbon nanotubes on the thermal conductivity of epoxy composites.* Mater Chem Phys 2011;126:722-8.
[33] Datsyuk V, Kalyva M, Papagelis K, Parthenios J, Tasis D, Siokou A, et al. *Chemical oxidation of multiwalled carbon nanotubes*. Carbon 2008;46:833-40.
[34] Dresselhaus MS, Dresselhaus G, Saito R, Jorio A. *Raman spectroscopy of carbon nanotubes.* Phys Rep 2005;409:47-99.

[35] Thomsen C, Reich C. *Double resonant Raman scattering in graphite.* Phys Rev Lett 2000;85:5214-7.
[36] Osswald S, Flahaut E, Ye H, Gogotsi Y. *Elimination of D-band in Raman spectra of double-wall carbon nanotubes by oxidation.* Chem Phys Lett 2005;402:422-7.
[37] Cummings A, Osman M, Srivastava D, Menon M. *Thermal conductivity of Y-junction carbon nanotubes*. Phys Rev B 2004;70:115405-1-6.
[38] Meng FY, Ogata S, Xu DS, Shibutani Y, Shi SQ. *Thermal conductivity of an ultrathin carbon nanotube with an X-shaped junction*. Phys Rev B 2007;75:205403-1-6.
[39] Sung YT, Han MS, Song KH, Jung JW, Lee Hs, Kum CK, et al. *Rheological and electrical properties of polycarbonate/multiwalled carbon nanotube composites*. Polymer 2006;47:4434-9.
[40] Lee SH, Cho ENR, Jeon SH, Youn JR. *Rheological and electrical properties of polypropylene composites containing functionalized multi-walled carbon nanotubes and compatibilizers*. Carbon 2007;45:2810-22.
[41] Hirsch A. *Functionalization of single-walled carbon nanotubes*. Angew Chem Int Ed 2002;41(11):1853-9.
[42] Kim SY, Baek SJ, Youn JR. *New hybrid method for simultaneous improvement of tensile and impact properties of carbon fiber reinforced composites*. Carbon 2011;49:5329-38.
[43] Kim JA, Seong DG, Kang TJ, Youn JR. *Effects of surface modification on rheological and mechanical properties of CNT/epoxy composites*. Carbon 2006;44:1898-905.

Chapter 3. Morphology and Physical Properties of Graphene Nanoplatelet Embedded Poly (Vinyl Alcohol) Aerogel

3.1. Introduction

Recently, carbon aerogels attract considerable attention by scientists as a new three-dimensional form of material with a wide range of applications, such as oil-absorption device [1-3], thermal insulator [4], gas sensor [5, 6], battery electrode [7], and supercapacitor [8-10]. Various types of carbon materials such as carbon nanotube (CNT) [11, 12], carbon nanofiber (CNF) [13, 14], graphene [15-17] have been introduced as the base material for the aerogel due to their superior mechanical, electrical, and morphological properties. For example, M. B. Bryning et al prepared CNT aerogels using wet-gel precursors and demonstrated that CNTs could be bound with the use of PVA [11]. Ye et al. fabricated graphene oxide/epoxy aerogel via the freeze-drying method [18]. In addition, Haiyan et al. reported a CNT/graphene hybrid aerogel with low density [19]. On the other hand, graphene nanoplatelets (GNPs), two-dimensional disc shaped particles, are produced by exfoliating natural graphite flake and have advantages such as lower cost and higher production rate than CNT or graphene [20].

It is important to control the internal structures of aerogel, including the fraction, size and the shape of pores since they determine the properties of the aerogel [21]. In general, the template based methods such as chemical vapor deposition (CVD) and physical vapor deposition (PVD) are two common methods to produce highly ordered structure. However, it is difficult to apply the template based methods to the commercial applications due to their complicated preparation procedure and high cost. On the other hand, a freeze-drying method

does not require any template and can be applied to mass production. In this respect, the freeze-drying method has been used for the fabrication of carbon aerogels. For instance, Kim et al. reported graphene coated CNT aerogel with extraordinary elasticity and fatigue resistance [22]. Furthermore, additional epoxy coating improved the mechanical properties of the aerogel [18].

In this study, we fabricated GNP/PVA aerogel using the freeze-drying method. The internal structure of the aerogel was manipulated by controlling the solvent composition and cross-linking the polymer. A mixture of water and ethanol was used as the solvent and maleic acid was used as the cross-linker. To the best of our knowledge, there was no report on the morphology control for aerogel by applying either solvent or cross-linker. The morphology of aerogel was identified with cryo-SEM and FE-SEM. The thermal conductivity and mechanical properties were evaluated. Moreover, the possibility of heat storage application with phase change materials was also investigated.

3.2. Experimental

3.2.1. Preparation of GNP/PVA Aerogel

GNPs (C grade) were purchased from XGScience (Michigan, USA) and had a true density of 2.2 g/cm^3 and a surface area of 750 m^2/g. PVA with a molecular weight of 89,000-98,000 and a degree of hydrolysis of 99+% and Maleic acid were supplied by Sigma Aldrich.

PVA was dissolved in DI water under vigorous stirring. The weight fraction of PVA was varied from 1.00 wt% to 2.00 wt%. The GNP powder was added to the PVA solution and suspended under sonication. The solution was poured into a cylindrical mold and quenched in the liquid nitrogen. Thereafter, the sample was freeze-dried for 48 h. Two different compositions of solvent were applied: one was pure DI water and the other was aqueous ethanol solution with a volume fraction of 20%. Maleic acid was mixed the GNP/PVA suspension with help of a mechanical stirrer. The content of maleic acid was 30% w/w PVA. After freeze-drying, the volume and mass of aerogel were measured directly. The porosity of aerogel was calculated by the following equation.

$$V_g = \frac{\rho_m - \rho_{air} - \rho_f}{\rho_m - \rho_{air}}, \tag{3.1}$$

where V_g denotes the porosity of aerogel, ρ_m is the density of the added materials, ρ_{air} is the density of air, and ρ_f is the density of aerogel. The experimental conditions, density, and porosity of the GNP aerogel are summarized in Table 3.1.

3.2.2. Characterization

The size distribution of GNPs in the suspension was analyzed with a dynamic light scattering spectrophotometer (DLS-7000, Otsuka Eletronics CO. Ltd, Japan). A cryogenic scanning electron microscope (Mira-3 FEG, Tescan, USA) was used to investigate the microstructure of the GNP suspension in liquid state. The frozen DI water suspension was sublimed at -100°C for 5 min after fracture, whereas the frozen DI

water/ethanol suspension was sublimed at -100°C for 10 min to prevent recrystallization of frozen water. The morphology of the GNP/PVA aerogel was observed with a scanning electron microscope (JSM-6390LV, JEOL, Tokyo, Japan) at room temperature. Fourier transform infrared attenuated total reflection spectroscopy (Nicolet 6700, Thermo Sciencific, Epsom, UK) was applied to identify the cross-linking reaction of PVA. The thermal conductivity of the aerogel was measured by using a thermal analyzer (C-Therm TCi, C-Therm Technologies Ltd, New Brunswick, Canada) based on a modified transient plane source method. The compressive strength was examined with a universal tensile test machine (Instron 3365, MA, USA) at room temperature.

Table 3.1. Density and porosity of the prepared GNP/PVA aerogels with respect to different experimental conditions.

Sample	PVA:GNP (weight ratio)	Solvent composition	Maleic acid (w/w PVA)	Density (g/cm3)	Porosity (%)
GP1	1:1	Water	-	0.0306	98.1
E-GP1	1:1	Water + EtOH	-	0.0131	99.2
GP2	2:1	Water	-	0.0974	93.4
X-GP2	2:1	Water	0.3	0.1170	92.2

3.3. Results & Discussion

3.3.1. Dispersion of GNP in suspensions

Dynamic light scattering (DLS), also known as photo correlation spectroscopy or quasi-elastic light scattering, is a technique used widely for analyzing the particle size and the size distribution [23]. This technique is based on the Brownian motion of spherical particles which causes a Doppler shift of incident laser light. The hydrodynamic diameter, d_h measured by using DLS, is presented in Fig. 3.1. The GNPs suspended in DI water had the mean diameter of about 900 nm, whereas those in the mixture of water and ethanol possessed a mean diameter of 360 nm. This discrepancy showed that the addition of ethanol led to a better dispersion of GNP in the suspension, which could affect the formation of ice crystal and then the microstructure of GNP/PVA aerogel. The enhanced particle dispersion could entail the generation of smaller pores and the improvement of porosity in the aerogel. Therefore, the E-GP1 aerogel shows higher porosity than the GP1 aerogel as listed in Table 3.1.

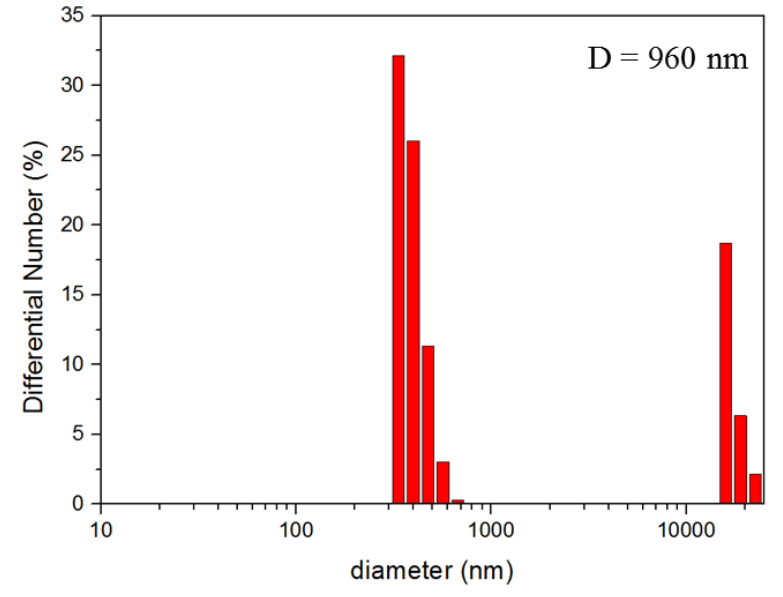

(a)

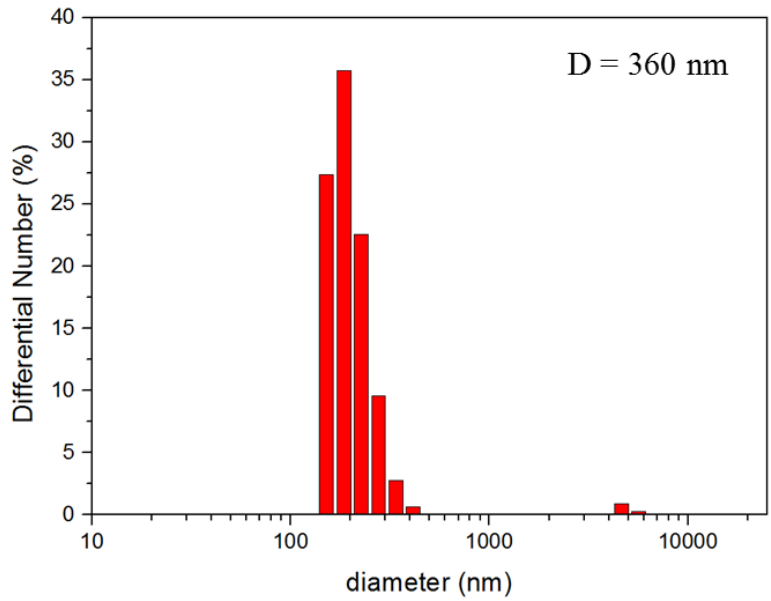

(b)

Figure 3.1. Distribution of the hydrodynamic particle diameter for GNPs suspended in (a) DI water and (b) aqueous ethanol solution with a volume fraction of 20%

3.3.2. Microstructure of Aerogel

The cryo-SEM observation was performed to investigate the internal structure of suspension in the liquid state. When the suspension sample was quenched with the use of liquid nitrogen, the heterogeneous nucleation sites were formed on the mold surface and ice crystals, which were larger than the critical size, were grown along with temperature gradient. Since the crystal growth along the c-axis of hexagonal ice was two orders of magnitude slower than the growth along the a-axis and b-axis, the lamellar structure of ice crystal was generated [24]. The GNPs were redistributed during the nucleation and the growth of ice crystal and relocated between the generated ice crystals. After freeze-drying, the ice crystals were sublimed, and the remained GNP particles formed lamella network structure with the organic binder. As a result, the ice crystal structure was transferred into the microstructure of the GNP/PVA aerogel [25].

Fig. 3.2(a) and 3.2(b) show cryo-SEM images of the GNP suspensions. The lamellar ice crystals were observed and the GNPs were placed between the ice crystals. It was found that the sample prepared with the water/ethanol mixture had smaller crystal size, i.e., closer interlayer distance of the ice crystals than the one prepared with DI water. This discrepancy in the crystal size was also observed for the pure DI water and the water-ethanol mixture without GNPs which are shown in Fig. 3.3. The addition of ethanol into water increased the number of nucleation sites and subsequently decreased the crystal size. Furthermore, the agglomerates of the GNPs were identified in Fig. 3.2(a). This implies relatively poor dispersion of the GNPs in water, which is in agreement with the aforementioned DLS result.

The SEM images of the GNP/PVA aerogels are presented in Fig. 3.4(a) and 3.4(b). Similar to the cryo-SEM observation, the water/ethanol mixture yielded more complicated microstructure with smaller pore than the DI water. It is worth noting that internal structural factors such as porosity, size, and shape of pore are determined by the

nature of solvent.

Fig. 3.5(a) and 3.5(b) demonstrate the effect of cross-linking of PVA with maleic acid on the microstructure of the aerogel. The solvent used was water, and the ratio of GNP and PVA was 1:2. The thickness of strut was increased after the cross-linking of maleic acid. The increase of strut could lead to an enhancement of the mechanical properties.

The change in the chemical structure is identified with the FT-IR spectra. Fig. 3.6 presents the spectra of the cross-linked GP2 aerogel. The characteristic peak of PVA was observed between 3,000 and 3,600 cm^{-1} due to the intermolecular and intramolecular hydrogen bonds [26, 27]. The peaks in the range of 2,910 through 2,942 cm^{-1} corresponded to the O-H and C-H stretching [28]. The peaks in between 1,430 and 1,446 cm^{-1} indicated the presence of the bending of O-H, C-H and CH_2 groups. In particular, for the cross-linked aerogel, a significant increase in the intensity of the peaks in the region of 1,610 and 1,710 cm^{-1} was detected. The cross-linking reaction of PVA with maleic acid forms the C=C, C=O, C-O-C, and –COOH groups. As a result, the occurrence of these groups leads to the conjugation of the functional groups and the shift of the peaks [29]. Additional evidence of the cross-linking reaction was the consumption of the O-H groups due to the esterification, which decreased the peak intensity of the functional group [30].

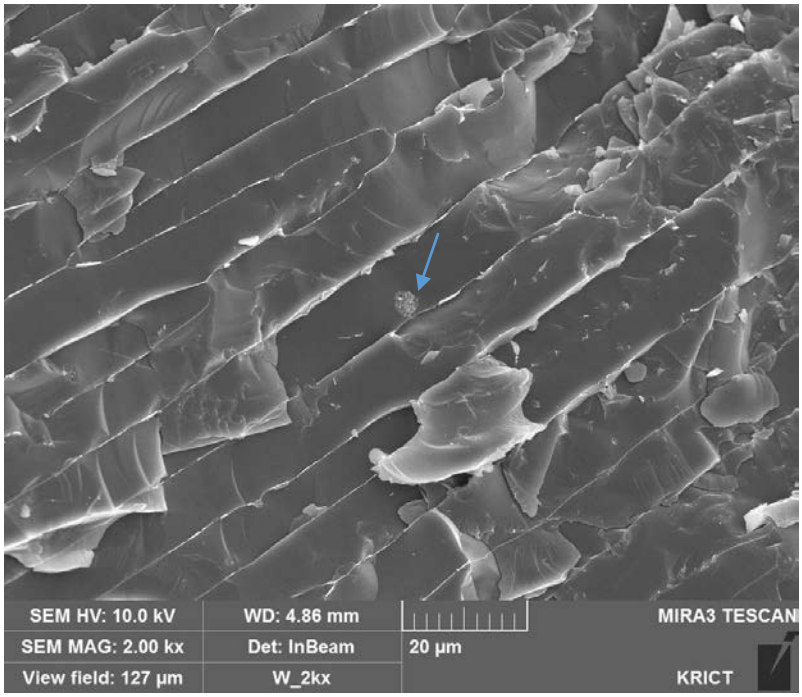

(a)

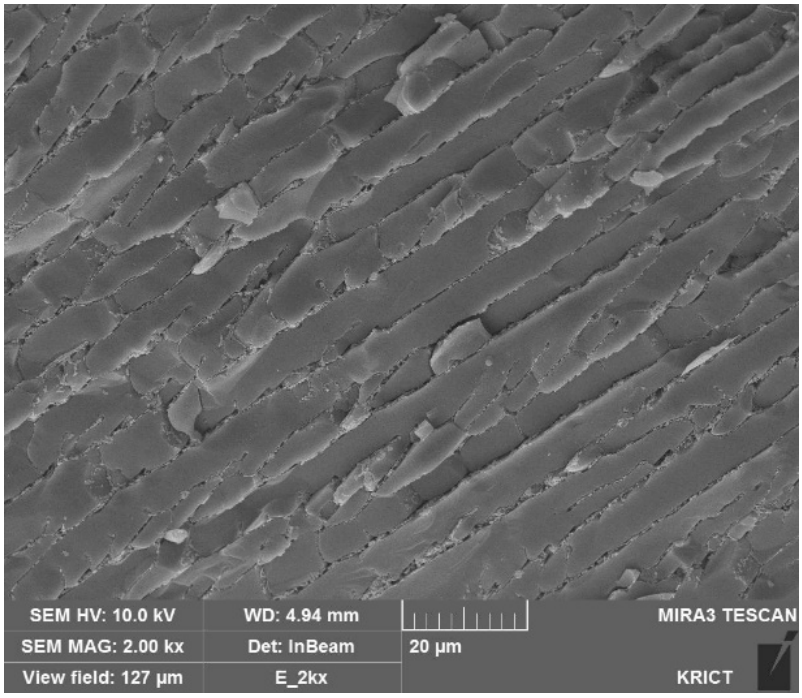

(b)

Figure 3.2. Cryo-SEM fracture images of frozen GNP suspensions: (a) DI water and (b) DI water/ethanol mixture.

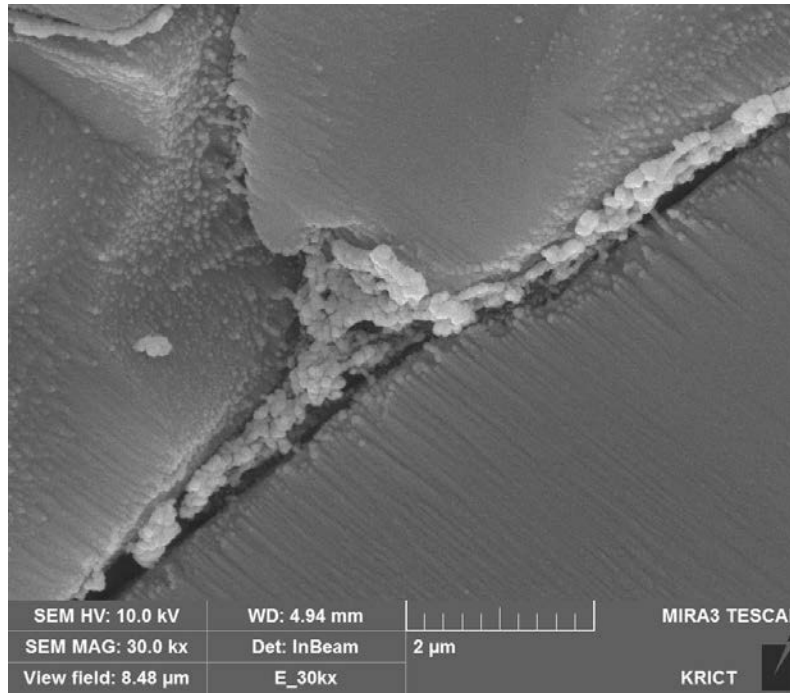

(a)

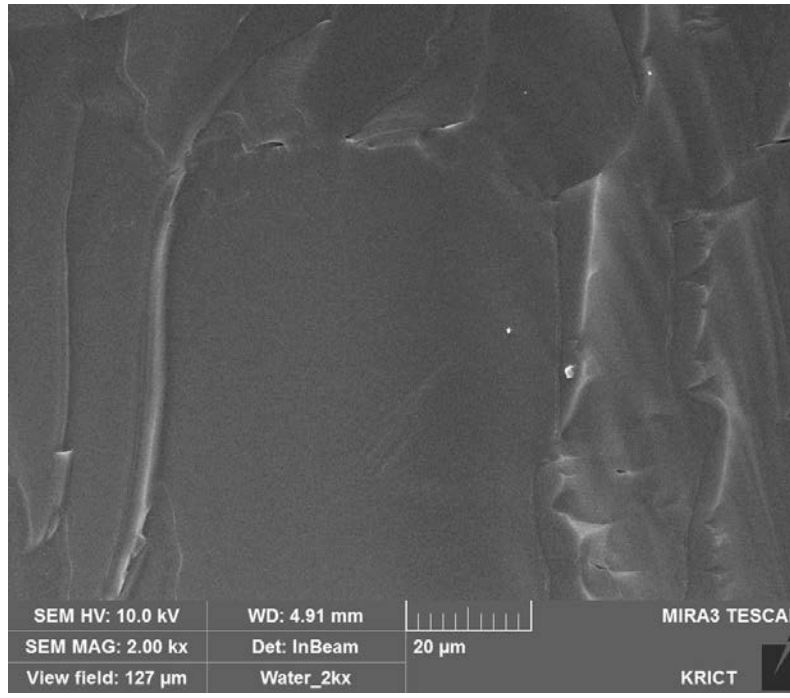

(b)

Figure 3.3. Cryo-SEM images of liquids: (a) DI water and (b) water/ethanol mixture.

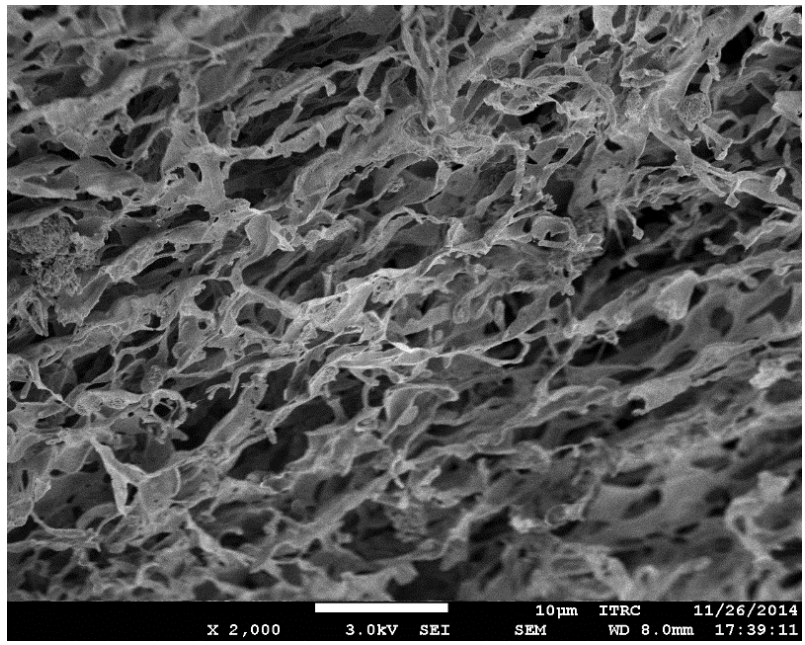

(a)

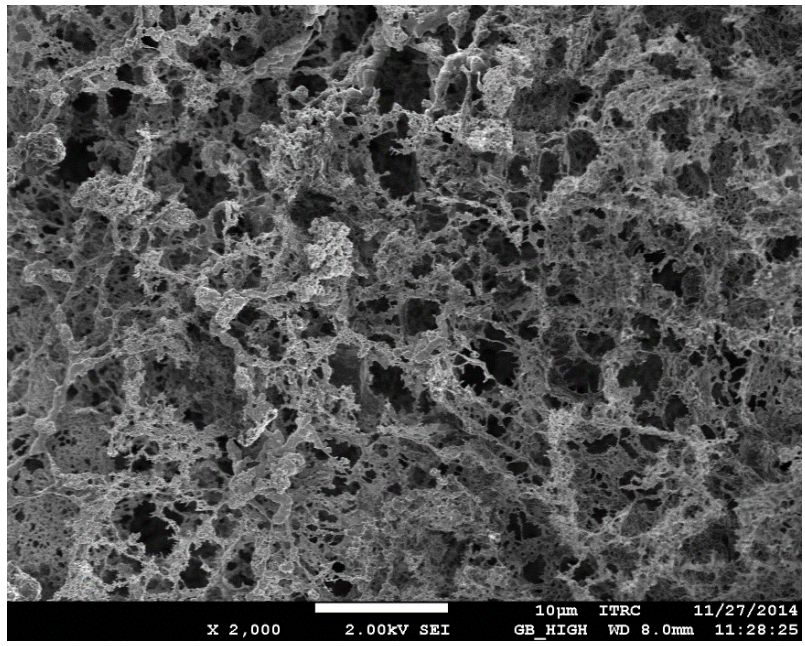

(b)

Figure 3.4. FE-SEM images of the internal structure of freeze-dried aerogels: (a) GP1 and (b) E-GP1.

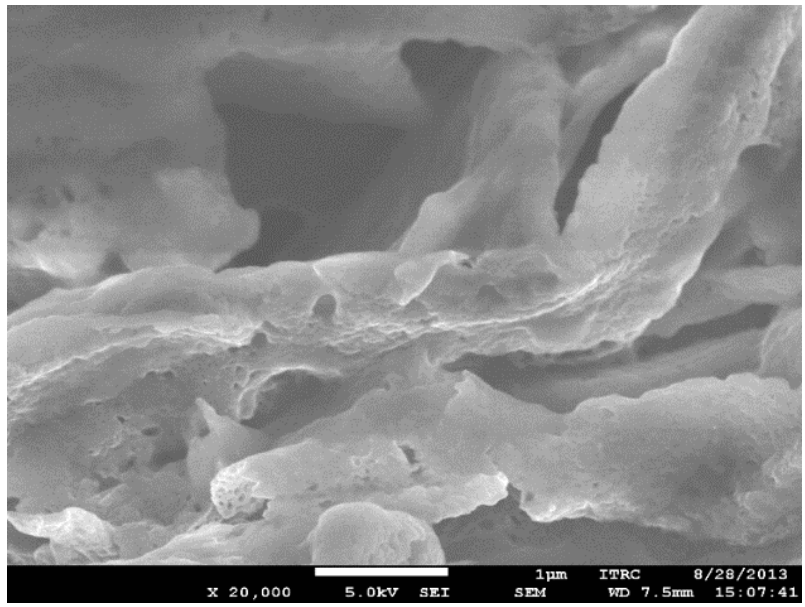

(a)

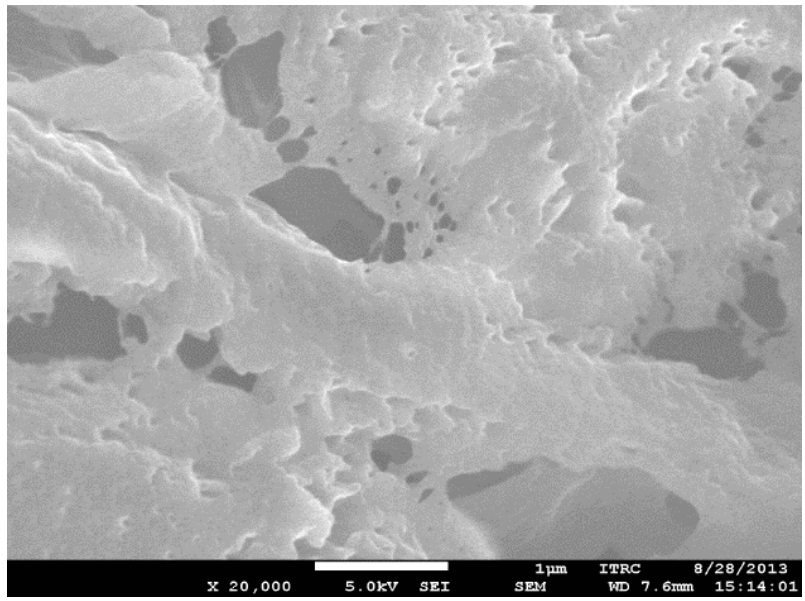

(b)

Figure 3.5. FE-SEM images of internal structure of freeze-dried aerogels: (a) GP2 and (b) X-GP2.

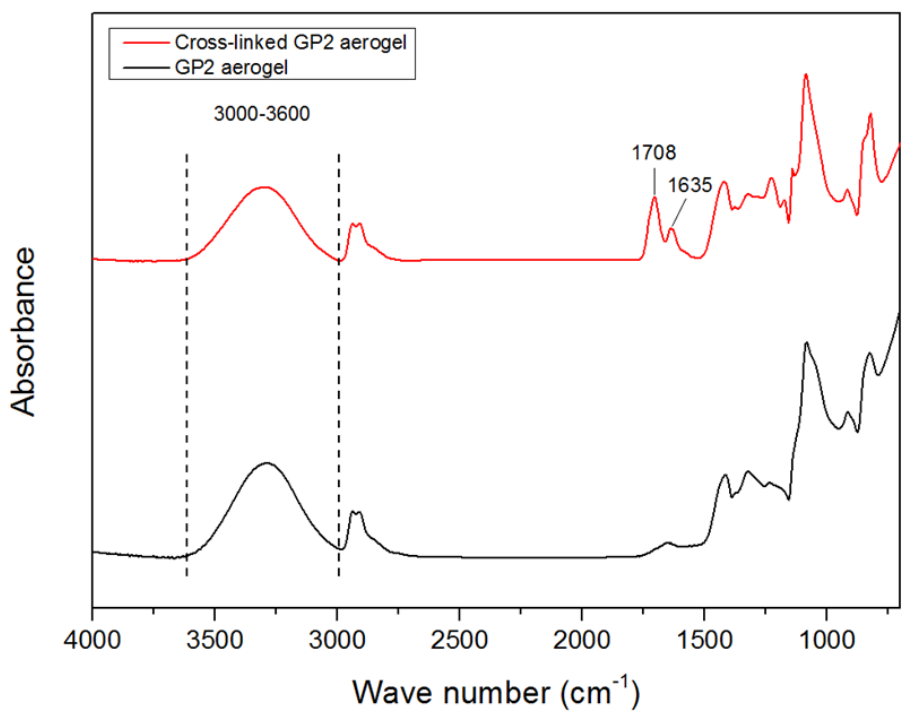

Figure 3.6. Comparison of the FT-IR spectra for GP2 aerogel and maleic acid cross-linked GP2 aerogel.

3.3.3. Thermal Conductivity

The thermal conductivity of the aerogel is presented in Fig. 3.7. As the porosity was increased, the thermal conductivity was decreased. This shows the fact that the porosity is a key factor of determining the thermal characteristics of aerogel. Heat is generally transferred through conduction, convection or radiation. It is reported that when the pore size is smaller than 4 mm, the convective heat transfer is negligible [31]. The thermal conductivity of the aerogel is decreased with increasing porosity due to the small thermal conductivity of air (i.e., 25 mW/m·K). The contribution of radiation to the overall heat transfer increases by 30~40% in a porous medium. In this sense, the pore size, an affecting factor of the radiation heat transfer, plays a crucial role in determining the thermal conductivity of aerogel. The radiative heat transfer is increased with the pore size increase. This is the reason why the E-GP1 aerogel had the smallest thermal conductivity. These results revealed that the thermal conductivity of aerogel can be manipulated by controlling the internal structure of aerogel.

3.3.4. Mechanical property

The strain-stress curves of GNP/PVA aerogels were shown in Fig. 3.8. Based on the s-s curves, Fig. 3.9 displays the specific compressive strength of the GNP/PVA aerogels at 80% strain. The aerogels with higher PVA content had better mechanical properties. The E-GP1 aerogel showed relatively small specific compressive strength because the aerogel with the micro-sized pores generated by using ethanol had significantly large porosity compared with the other samples. The specific compressive strength was maximized when cross-linking was applied to the aerogel, i.e., X-GP2. This result can also be explained by considering the change of the strut thickness which was observed from the SEM experiment.

3.3.5. Stability in Aqueous Environment

To exploit the stability of the aerogels in aqueous environment, the GP2 aerogel and X-GP2 aerogel were immersed in DI water for 10 min. As shown in Fig. 3.10, the cross-linked aerogel maintained its original structure in the water, whereas the structure of the GP2 aerogel was broken due to the dissolution of PVA in the water. This observation showed that the PVA cross-linked with maleic acid could have structural stability in aqueous liquid. We anticipate that the cross-linking of polymeric GNP aerogels will allow the usage of the aerogels in aqueous environment.

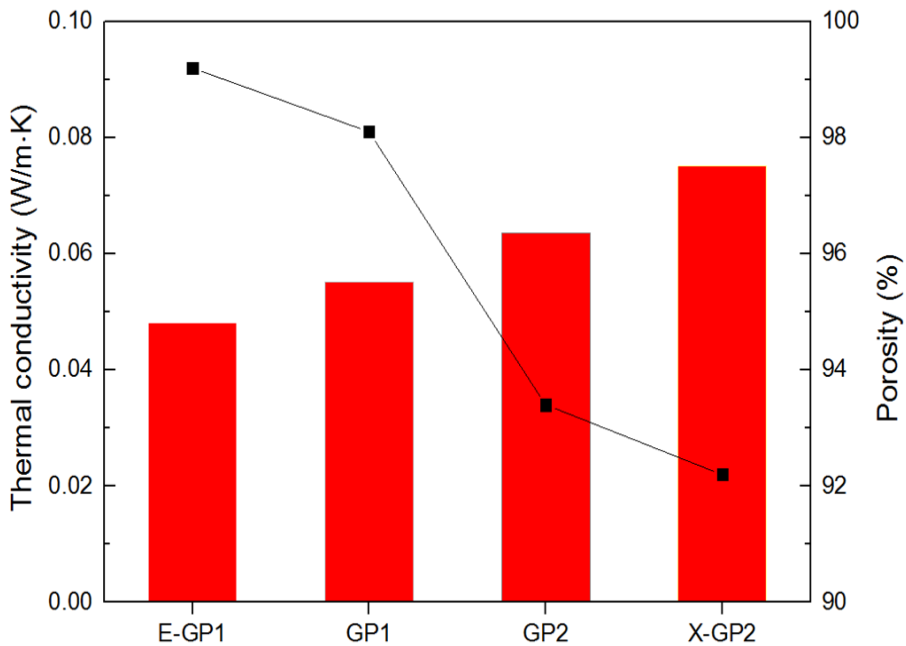

Figure 3.7. Thermal conductivity and porosity of GNP/PVA aerogels.

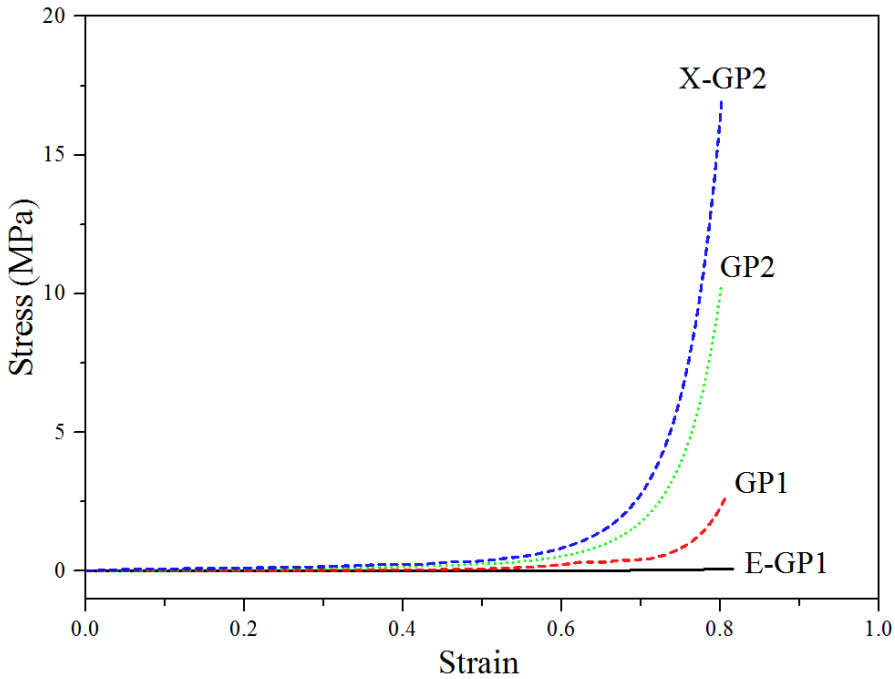

Figure 3.8. The strain-stress curves of the GNP/PVA aerogels.

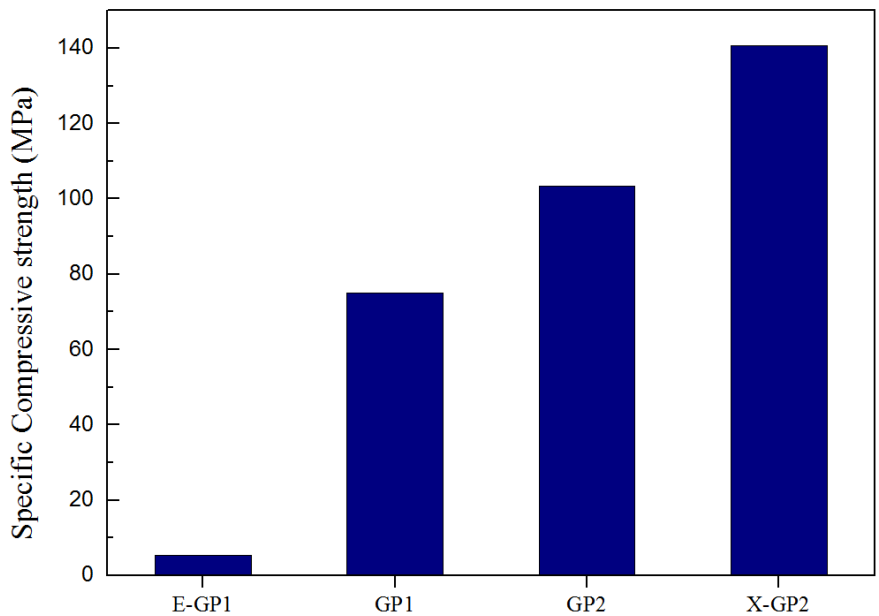

Figure 3.9. Specific compressive strength of the GNP/PVA aerogels at 80% strain.

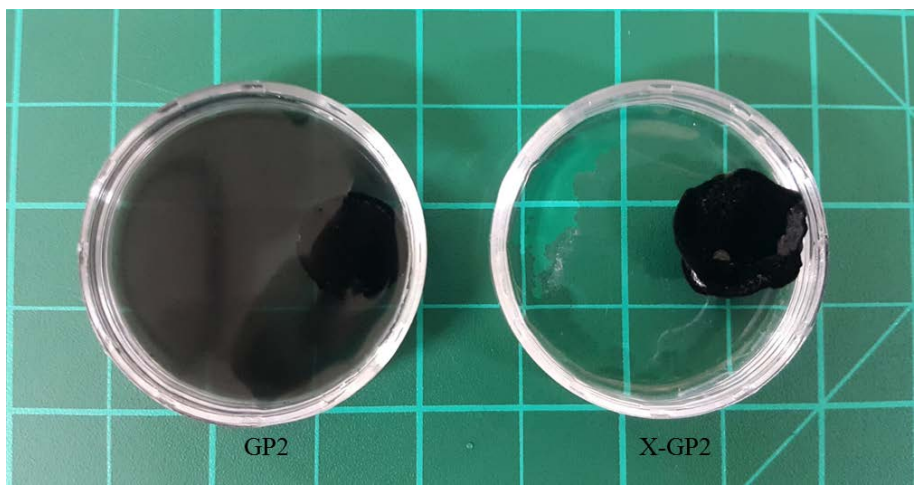

Figure 3.10. Stability of the GP2 aerogel and X-GP2 aerogel in aqueous environment.

3.4. Application of GNP Embedded PVA Aerogel

3.4.1. Shape-Stability

In order to apply the GNP embedded PVA aerogel for the heat storage device, the shape of composite should be sustainable at melting temperature of PEG (phase change material used in present study). Fig. 3.11 displays the optical images of shape-stability test of neat PEG and PEG impregnated E-GP1 aerogel (PEG/E-GP1). The melting of the PEG was already started at 50 ^{o}C. Then, the PEG was completely melted and its structure was collapsed at 80 ^{o}C. On the other hands, the PEG/E-GP1 maintained its original shape at 80 ^{o}C and leakage of PEG was not observed in Fig 3.11. This excellent shape-stability of the PEG/E-GP1 is attributed to strong interaction between the PEG and the E-GP1 aerogel, allowing the GNP embedded PVA aerogel to be applied to the heat storage device. Moreover, the interconnected network structure of the E-GP1 aerogel is also because of the outstanding shape-stability of PEG/E-GP1.

3.4.2. DSC Thermal Spectra

The heat storage capacity is very important property for evaluating of the heat storage performance of the phase change materials having a significant value of the latent heat of fusion [32]. Differential scanning calorimetry is a typical characterization method to measure the heat storage capacity. The heat flow curves for the neat PEG and the PEG/E-GP1 was shown in Fig. 3.12. The melting and freezing heat flow curves for the neat PEG present the exothermic peaks centered at 37-39 ^{o}C and the endothermic peaks centered at 68-70 ^{o}C, corresponding to the freezing temperature and melting temperature of the neat PEG, respectively. The DSC curves for the PEG/E-GP1 shows the slightly shifts of exothermic and endothermic peak, indicating the melting temperature of PEG/E-GP1 was shifted to 65-67 ^{o}C and the freezing temperature was lowered to 36-38 ^{o}C. These slight shifts of phase

change temperature are probably due to the confinement effect of the three-dimensional graphene nanoplatelets network [33]. The latent heat of melting and freezing for the PEG/E-GP1also decreased from 172.89 J/g and 155.94 J/g to 169.6 J/g and 151.16 J/g, respectively. The thermal storage capacity rates (η), representative index for the heat storage capacity, are defined as the ratio of latent heat of melting of the PEG/E-GP1 to that of the neat PEG and listed in Table 3.2. This result revealed that the thermal storage capability rate (96.9%) of PEG/E-GP1 is comparable to that of the neat PEG. The latent heat of fusion is independent on the existence of the E-GP1 aerogel due to its low density and high surface area, while the shape stability is enhanced.

3.4.3. Thermoelectric Effectivity

Thermoelectric devices generate the electric energy by using the heat energy from the heat storage part through the transferring the heat. The advanced PCM, PEG/E-GP1, can be used as the part for collecting and storing heat energy in a thermoelectric generator device. The mechanism of the energy harvesting is based on the Seebeck effect which were bound to the generation of electric energy with temperature difference between a colder side and a hotter side of device [34]. A Scheme of thermoelectric device with PEG/aerogel composite was illustrated in the Fig. 3.13. The Heat sink was replaced by ice water, which help the lower side of device keep a constant temperature corresponding to 0 ^{o}C, and advanced PCM was used for the heat source. Fig. 3.14a shows the generated electric current (I) as a function of time (t) of thermoelectric device with and without advanced PCM. Compared to the I-t curve of a sample, which is filled with epoxy instead of PEG, the thermoelectric device with the advanced PCM shows a longer plateau of steady-state current and time delay due to the large heat storage capacity of the PEG. This result agrees well with the temperature (T) curve as a function of time (t) shown in Fig. 3.14b. The temperature of the epoxy was rapidly dropped from the beginning of

the measurement. However, the temperature of the PEG/E-GP1 sustained 40 ºC corresponding to the freezing temperature of the PEG for long time. These results indicated that the GNP embedded PVA aerogel could be applied to the heat storage part in the energy harvesting devices.

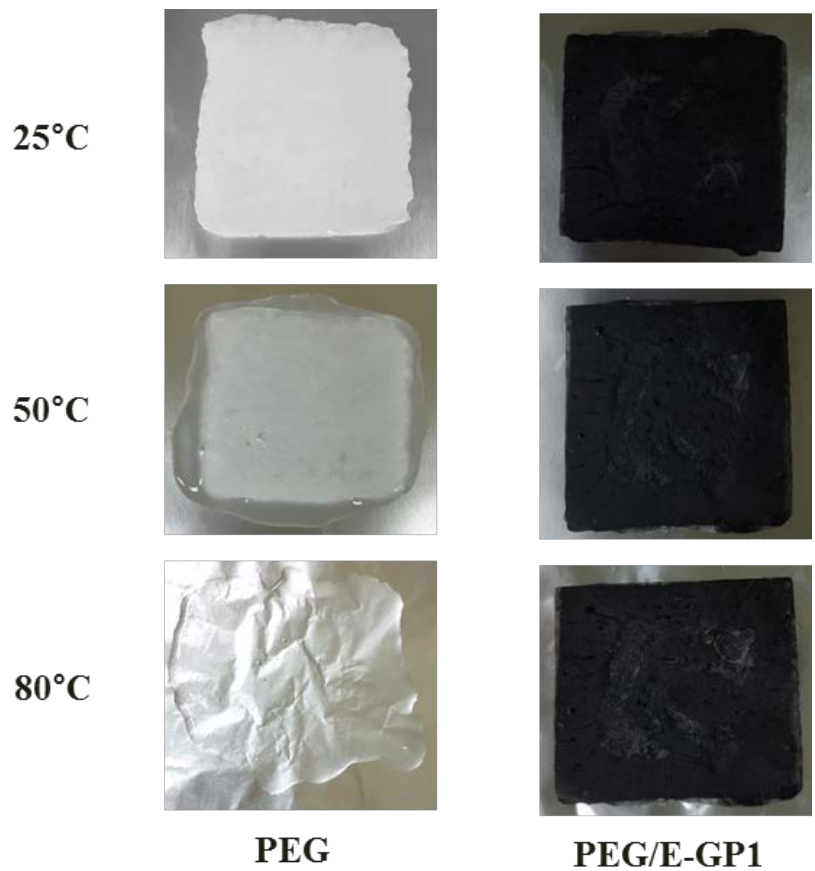

Figure 3.11. Shape-stability test of PEG and PEG/E-GP1.

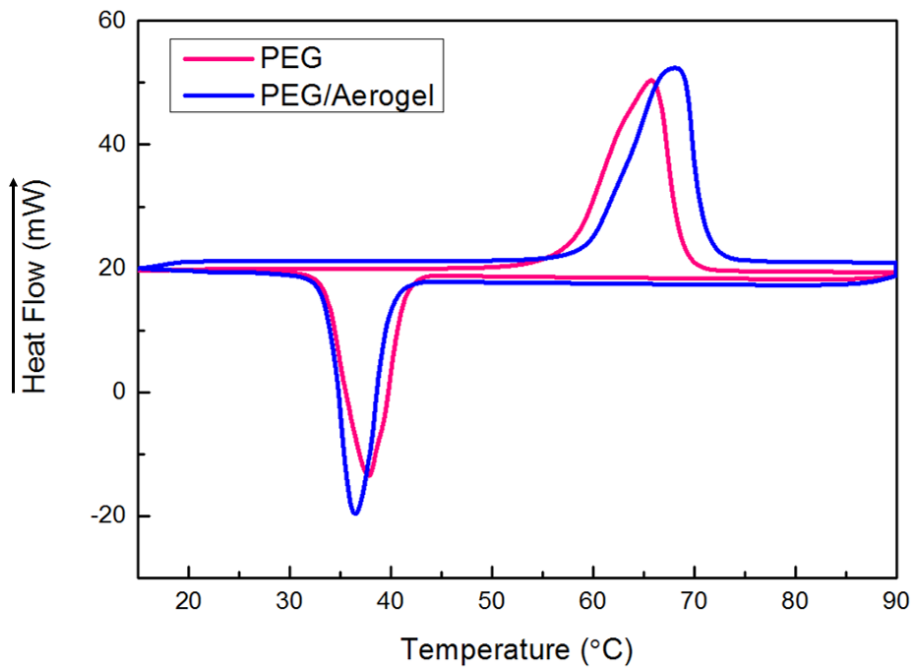

Figure 3.12. DSC thermal spectra of PEG and PEG/E-GP1 composite.

Table 3.2. Melting temperature (T_m), freezing temperature (T_f), latent heats of melting (ΔH_m), latent heat of freezing (ΔH_f), and thermal storage capability rate (η) for PEG and PEG/E-GP1 composite.

Sample	T_m (℃)	T_f (℃)	ΔH_m (J/g)	ΔH_f (J/g)	η
PEG	65.7	37.8	172.89	155.94	100
PEG/ E-GP1	67.5	36.7	169.6	151.16	96.9

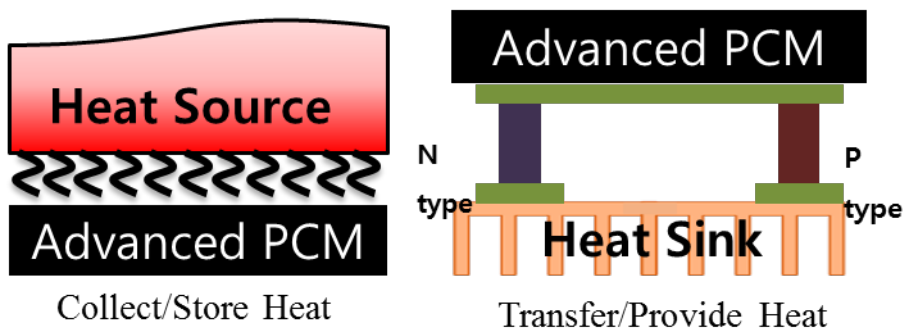

Figure 3.12. A Scheme of thermoelectric device with PEG/E-GP1 composite as the advanced PCM.

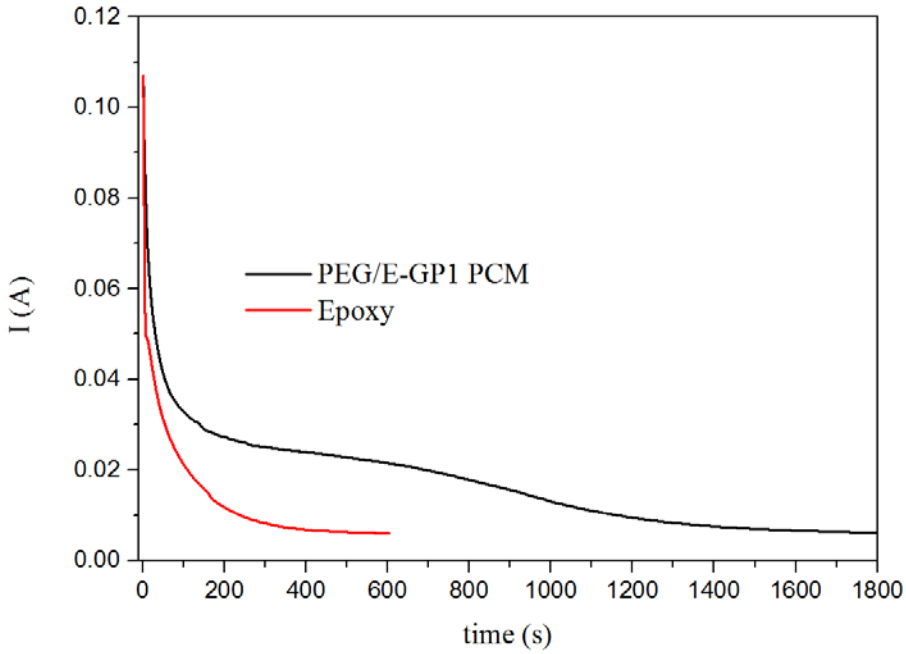

(a)

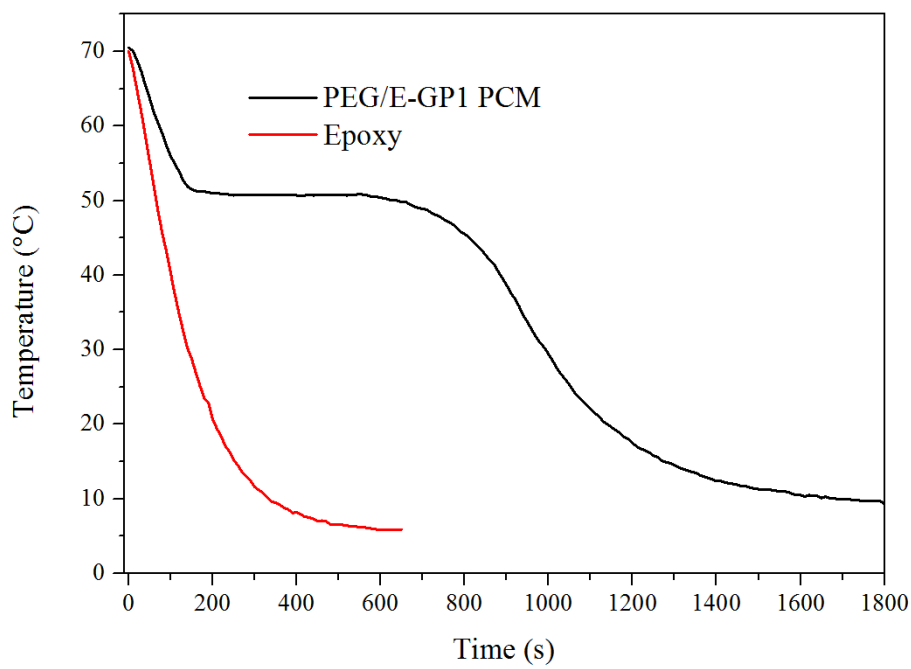

(b)

Figure 3.13. (a) *I-t* curves of PEG/E-GP1 composite and epoxy and (b) *T-t* curves of PEG/E-GP1 composite and epoxy.

3.5. Summary

GNP embedded PVA aerogels were prepared and their thermal and mechanical properties were investigated. The internal structure of the composite aerogel was controlled by changing the solvent composition and applying the chemical treatment to the aerogels. When ethanol was added to the solvent, the porosity was increased and thus thermal conductivity of the GNP aerogel was diminished. The cryo-SEM observation was carried out to examine the formation and the growth of ice crystal during freeze-drying, which determined the internal structure of the aerogel. The cross-linking of the aerogel enhanced the mechanical property and stability in the water. This study can provide a promising way of controlling the morphology of GNP aerogel in a simple and systematic manner and expand its applications.

3.6. References

[1] S. Kabiri, D. N. H. Tran, T. Altalhi, and D. Losic, *Outstanding adsorption performance of graphene–carbon nanotube aerogels for continuous oil removal*, Carbon 2014;80:523–533.

[2] Y. He, Y. Liu, T. Wu, J. Ma, X. Wang, Q. Gong, et al., *An environmentally friendly method for the fabrication of reduced graphene oxide foam with a super oil absorption capacity*, Journal of hazardous materials 2013;260:796–805.

[3] LI, Jihao, et al. *Ultra-light, compressible and fire-resistant graphene aerogel as a highly efficient and recyclable absorbent for organic liquids*. Journal of Materials Chemistry A, 2014, 2.9: 2934-2941.

[4] B. Wicklein, A. Kocjan, G. Salazar-Alvarez, F. Carosio, G. Camino, M. Antonietti, et al., *Thermally insulating and fire-retardant lightweight anisotropic foams based on nanocellulose and graphene oxide*, Nature nanotechnology 2015;10:277–283.

[5] W. Yuan and G. Shi, *Graphene-based gas sensors*, Journal of Materials Chemistry 2013;1:10078–10091.

[6] L. Li, S. He, M. Liu, C. Zhang, and W. Chen, *Three-dimensional mesoporous graphene aerogel-supported SnO2 nanocrystals for high-performance NO2 gas sensing at low temperature*, Analytical chemistry 2015;87:1638–1645.

[7] Z.-L. Wang, D. Xu, H.-G. Wang, Z. Wu, and X.-B. Zhang, *In situ fabrication of porous graphene electrodes for high-performance energy storage*, Acs Nano 2013;7:2422–2430.

[8] D. Kalpana, K. Omkumar, S. S. Kumar, and N. Renganathan, *A novel high power symmetric ZnO/carbon aerogel composite electrode for electrochemical supercapacitor*, Electrochimica Acta 2006;52: 1309–1315.

[9] J. Li, X. Wang, Q. Huang, S. Gamboa, and P. Sebastian, *Studies on preparation and performances of carbon aerogel electrodes for the application of supercapacitor*, Journal of Power Sources 2006;158: 784–788.

[10] S. Kim, S. Hwang, and S. Hyun, *Preparation of carbon aerogel*

electrodes for supercapacitor and their electrochemical characteristics, Journal of materials science 2005;40:725-731.
[11] M. B. Bryning, D. E. Milkie, M. F. Islam, L. A. Hough, J. M. Kikkawa, and A. G. Yodh, *Carbon nanotube aerogels*, Advanced Materials 2007;19:661-664.
[12] J. Zou, J. Liu, A. S. Karakoti, A. Kumar, D. Joung, Q. Li, et al., *Ultralight multiwalled carbon nanotube aerogel*, Acs Nano 2010;4: 7293-7302.
[13] Q. Zheng, Z. Cai, and S. Gong, *Green synthesis of polyvinyl alcohol (PVA)-cellulose nanofibril (CNF) hybrid aerogels and their use as superabsorbents*, Journal of Materials Chemistry A 2014;2:3110-3118.
[14] H. Bi, Z. Yin, X. Cao, X. Xie, C. Tan, X. Huang, et al., *Carbon fiber aerogel made from raw cotton: a novel, efficient and recyclable sorbent for oils and organic solvents*, Advanced Materials 2013;25:5916-5921.
[15] M. A. Worsley, P. J. Pauzauskie, T. Y. Olson, J. Biener, J. H. Satcher Jr, and T. F. Baumann, *Synthesis of graphene aerogel with high electrical conductivity*, Journal of the American Chemical Society 2010;132:14067-14069.
[16] H. Hu, Z. Zhao, W. Wan, Y. Gogotsi, and J. Qiu, *Ultralight and highly compressible graphene aerogels*, Advanced materials 2013;25:2219-2223.
[17] M. A. Worsley, T. T. Pham, A. Yan, S. J. Shin, J. R. Lee, M. Bagge-Hansen, et al., *Synthesis and characterization of highly crystalline graphene aerogels*, Acs Nano 2014;8:11013-11022.
[18] S. Ye, J. Feng, and P. Wu, *Highly elastic graphene oxide-epoxy composite aerogels via simple freeze-drying and subsequent routine curing*, Journal of Materials Chemistry A 2013;1:3495-3502.
[19] H. Sun, Z. Xu, and C. Gao, *Multifunctional, ultra-flyweight, synergistically assembled carbon aerogels*, Advanced Materials 2013;25:2554-2560.
[20] H. Fukushima and L. Drzal, *Graphite nanoplatelets as reinforcements for polymers: structural and electrical properties," in Proceedings of the 17th Annual Conference of the American Society*

for Composites, Purdue University, West Lafayette, IN, 2002.
[21] Z. Chen, W. Ren, L. Gao, B. Liu, S. Pei, and H.-M. Cheng, *Three-dimensional flexible and conductive interconnected graphene networks grown by chemical vapour deposition*, Nature materials 2011;10:424-428.
[22] K. H. Kim, Y. Oh, and M. Islam, *Graphene coating makes carbon nanotube aerogels superelastic and resistant to fatigue*, Nature nanotechnology;7:562-566.
[23] B. J. Berne and R. Pecora, *Dynamic light scattering: with applications to chemistry, biology, and physics*: Courier Corporation, 1976.
[24] V. F. Petrenko and R. W. Whitworth, *Physics of ice*: Clarendon Press, 1999.
[25] S. Deville, E. Saiz, and A. P. Tomsia, *Ice-templated porous alumina structures*, Acta Materialia 2007;55:1965-1974.
[26] F. Senti and D. Harker, *The crystal structure of rhombohedral acetamide*, Journal of the American Chemical Society 1940;62: 2008-2019.
[27] D. Hall and F. Llewellyn, *The crystal structure of formamidoxime*, Acta Crystallographica 1956;9:108-112.
[28] H. Mark, Encyclopedia of Polymer Science and Technology, 12 Volume Set: John Wiley & Sons, Inc, 2005.
[29] X. H. Qin and S. Y. Wang, *Electrospun nanofibers from crosslinked poly (vinyl alcohol) and its filtration efficiency*, Journal of applied polymer science 2008;109:951-956.
[30] M. S. Peresin, A. H. Vesterinen, Y. Habibi, L. S. Johansson, J. J. Pawlak, A. A. Nevzorov, et al., *Crosslinked PVA nanofibers reinforced with cellulose nanocrystals: water interactions and thermomechanical properties*, Journal of Applied Polymer Science 2014;131.
[31] R. Skochdopole, *The thermal conductivity of foamed plastics*, Chem. Eng. Prog 1961;57:55-59.
[32] AGYENIM, Francis, et al. *A review of materials, heat transfer and phase change problem formulation for latent heat thermal energy storage systems (LHTESS).* Renewable and sustainable energy

reviews, 2010, 14.2: 615-628.
[33] ALBA-SIMIONESCO, C., et al. *Effects of confinement on freezing and melting*. Journal of Physics: Condensed Matter, 2006, 18.6: R15.
[34] SHARMA, Sudhanshu; DWIVEDI, V. K.; PANDIT, S. N. *A review of thermoelectric devices for cooling applications*. International journal of green energy, 2014, 11.9: 899-909.

Chapter 4. The Fabrication of Lightweight and Mechanically Enhanced Core-Shell Structured Epoxy/rGO Composite.

4.1. Introduction

Three dimensional network of carbon aerogel provides a great potential for use in various engineering fields, considering the extraordinary properties of carbon nanomaterial. The carbon network is constructed by interconnection of carbon nanomaterials with the use of binding material which plays an important role in maintaining the stable shape of carbon aerogel [1, 2]. However, recently reported a self-supported binder free graphene oxide (GO) aerogel exhibited enhanced mechanical performance and remarkable shape-stability [3]. The outstanding shape-stability is attributed to Van der Waals forces between the oxygenated functional groups on the GO surface and physical interlocking between the GO sheets. However, the applications of GO aerogel are limited due to the poor surface hardness of aerogel structure.

The outstanding physical properties of two dimensional graphene have been studied by many researchers after the discovery of mechanical exfoliation method to obtain a single layer graphene sheet [4]. Reduced graphene oxide (rGO), prepared by oxidation and reduction of graphite, is a kind of the graphene and has a number of advantages including the simple process, the suitability for scalable production, and the relatively low fabrication cost. Therefore, a variety of oxidation methods have attracted a keen interest for fabricating reduced graphene oxide [5-7]. Although the physical properties of rGO are lagging behind those of the single layer graphene due to the presence of defect and disorder on the reduced graphene oxide, a variety of rGO/polymer composites possessing the enhanced electrical and

mechanical performances have been reported [8, 9]. However, the enhancement of thermal conductivity of rGO/polymer composite was not significant [10]. The discrepancy between the electrical and thermal conductivity of the rGO/polymer composite allows in application in thermoelectric device [11, 12].

In this study, we fabricated the epoxy/rGO composite by infiltrating an epoxy resin into the rGO aerogel for the purpose of enhancing the surface hardness of the aerogel, thereby expand the usage of the aerogel. Moreover, the core-shell structure is proposed in order to sustain the low density and large surface area of rGO aerogel. Two different core-shell structured epoxy/rGO composites were prepared by making difference in epoxy infiltration time. The effect of infiltration time on the physical properties including density, surface hardness, thermal conductivity and electrical conductivity were also investigated. We expected that present study provide a pathway towards fabricating lightweight and mechanically enhanced epoxy/rGO composites.

4.2. Experimental

4.2.1. Materials

The mixture of epoxy resin (KER 9200, Kumho P&B chemicals, Korea) and its hardener (KCA 9220, Kumho P&B chemicals, Korea) has relatively low viscosity which was appropriate for polymer infiltration into carbon aerogel. Graphite flake, $K_2S_2O_8$, P_4O_{10} and $KMnO_4$ were purchased from Sigma-Aldrich. And H_2SO_4, H_2O_2 and HCl were supplied from Daejung Chemicals & metals.

4.2.2. Synthesis of Graphene Oxide (GO)

Graphene oxide (GO) was synthesized from graphite flake by using modified Hummer`s method [13]. Pre-oxidation of the graphite flake with $K_2S_2O_8$ and P_4O_{10} was employed in order to enhance the yield of the graphite flake. Then, 3.0 g of pre-oxidized graphite was dispersed into 138 mL of H_2SO_4 that had been cooled to 0 ^oC in advance. 18.0 g of KMnO4 was then slightly added so as to prevent the mixture temperature from rising above 10 ^oC. The mixture was stirred at 35 ^oC for 2 hours and resulting mixtures was diluted by adding 276 mL of DI water under vigorous stirring. Then, the mixture was transferred to an ice bath and mixed with 5 mL of H_2O_2 to ensure the completion of reaction with $KMnO_4$. The resulting mixture was washed with HCl and DI water respectively, followed by filtration. In order to neutralize the mixed solution, the mixture was centrifuged at 13,000 rpm and diluted with DI water until the pH of the solution reached a suitable pH range. The graphene oxide powder was obtained after freeze-drying of the centrifuged solution for 2 days.

4.2.3. Preparation method

Firstly, 10.0 mg of the GO powder was dispersed into 10 mL of DI water. Simple mixing by using stirring and sonication resulted in the

formation of a solution containing highly dispersed GO. Then, the GO solution was transferred to previously prepared cylindrical mold and quenched in the liquid nitrogen. The GO aerogel was obtained after freeze-drying for 2 days. Reduction of GO aerogel was performed in hydrazine hydrate vapor for 24 hours. Epoxy resin and curing agent were mixed and degassed in vacuum oven for 30 min. The infiltration of the mixture of epoxy resin and curing agent into rGO aerogel was followed. In order to fabricate the core-shell structure of epoxy/rGO aerogel composite, the infiltration was carried out for relatively short period of time. The experimental condition and dimension of the prepared samples were listed in Table 4.1.

Table 4.1. Dimension and physical properties of core shell epoxy/rGO composites.

	Sample 1	Sample 2
Infiltration time	3 min	10 min
Radius (cm)	0.964	0.9435
Thickness (cm)	0.501	0.486
Volume fraction of rGO aerogel	0.728	0.222
Density (g/cm^3)	0.435	1.001

4.2.4. Characterization

Field-emission scanning electron microscopy (FE-SEM) was employed in order to observe the morphology of the core-shell structured epoxy/rGO composite. Fractured surfaces of the core-shell composite were coated with platinum in vacuum oven for 300 s by using a sputter coating machine. Thermal conductivity of the epoxy/rGO composite was measured with a thermal analyzer (C-therm, Tci, C-Therm Technologies Ltd, New Brunswick, Canada) which is a kind of thermal conductivity measurement method based on the modified transient plane source method. However, the thermal analyzer was not suitable method for measuring the thermal conductivity of the core-shell structured epoxy/rGO composite due to its heterogeneous core-shell structure. Therefore, the effective thermal conductivity of the core-shell structured epoxy/rGO composite was calculated from a temperature distribution of the prepared samples as a function of time and heat transfer coefficient. In order to measure the temperature of samples as a function of time, the samples were placed on a hot plate at a constant temperature of 70 ^{o}C for 10 min. The temperature of samples was recorded by IR camera (VT-2, FLUKE) during the measurement. The heat transfer coefficient was estimated by using finite element analysis. Surface hardness of the core-shell structured epoxy/rGO composite was measured by Vickers hardness test machine (HM-210, Mitutoyo, Japan). The kilograms-force per square millimeter (kgf/mm2) were maintained at 30 kgf/mm^2 for 10 seconds. Two-point probe method were carried out to measure the electrical conductivity of the prepared samples.

4.3. Results & Discussion

4.3.1. Morphology

Fig. 4.1 present the morphology of the rGO aerogel and the core-shell structured epoxy/rGO composites. The wrinkled surface textures of rGO sheets, which is shown in Fig. 4.1a and 4.1b, play the crucial role in constructing the three-dimensional (3D) network of rGO aerogel, allowing the stable structure of aerogel. Fig. 4.1c shows the cross-section of the core-shell structured epoxy/rGO composite. The fracture surface of the epoxy/rGO composite shell was found to have more smooth than that of the rGO aerogel core. SEM image shown in Fig. 4.1d further confirm the heterogeneous structure of the core-shell composite. Compared with the shell structure observed on the left side of SEM image, the three-dimensional network structure was well preserved at the core structure shown on the right side of SEM image. From this result, we might infer that the rGO aerogel maintained its original shape after infiltration of epoxy into the aerogel, resulting in relatively low density of the core-shell structured epoxy/rGO composite.

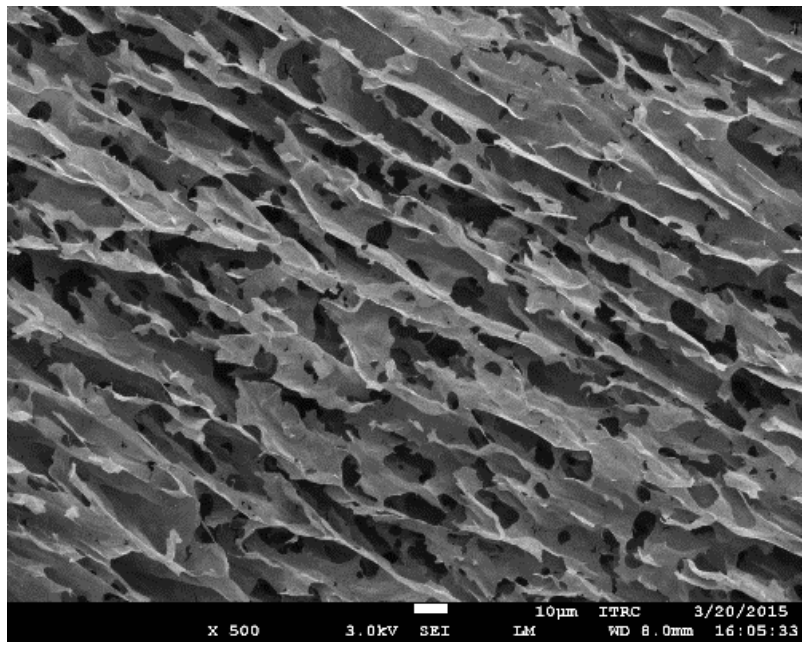

(a)

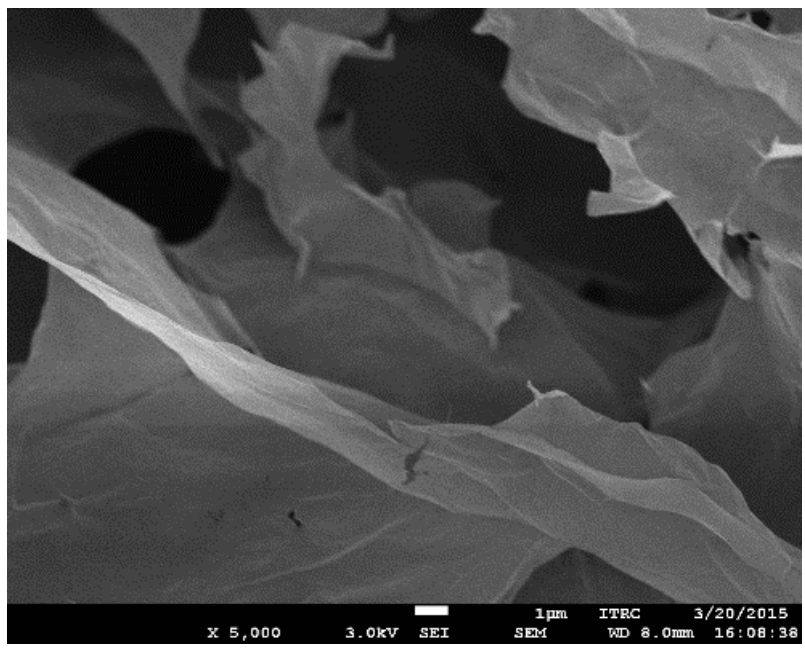

(b)

Figure 4.1. FE-SEM images of (a) network structure of rGO aerogel, (b) wrinkled structure of rGO sheets, (c) cross-section of the core-shell epoxy/rGO composite, and (d) magnified view of the border line between the aerogel core and the composite shell.

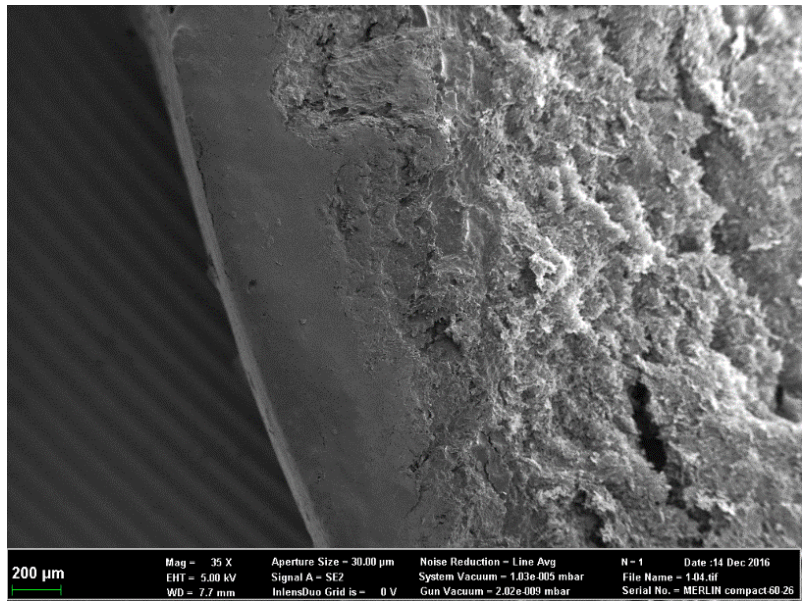

(c)

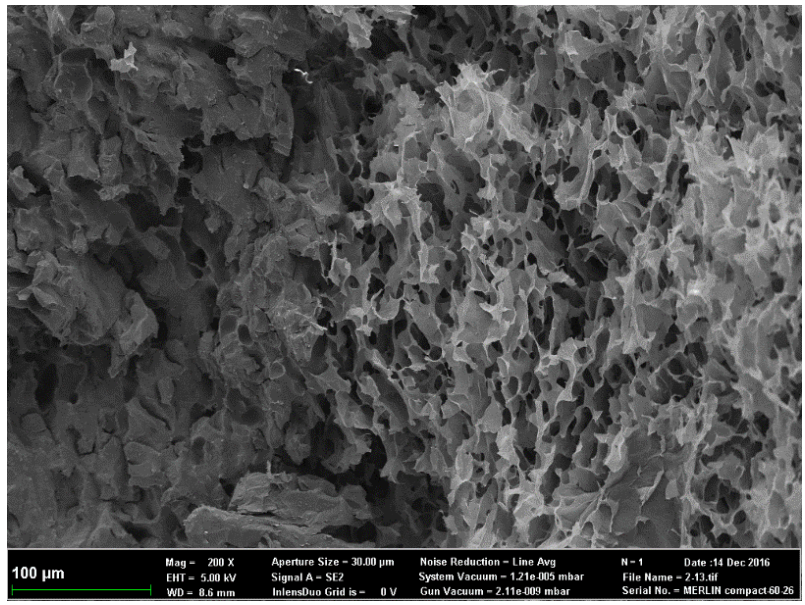

(d)

Figure 4.1. (Continued)

4.3.2. Thermal Conductivity of Epoxy/rGO and rGO Aerogel.

Thermal conductivity of the rGO aerogel was measured by modified transient plane source method. Although the thermal conductivity of single layer graphene sheet is 3,000 W/m·K, the thermal conductivity of the rGO aerogel is only 0.043 W/m·K, corresponding to the thermal conductivities of thermally insulating materials such as poly urethane foam or poly styrene foam [14, 15]. Thermal conductivity of the epoxy/rGO composite prepared by vacuum infiltration and solution mixing were also measured respectively. In the case of epoxy/rGO composite prepared by vacuum infiltration, the epoxy resin was infiltrated for 2 hours in the vacuum oven. Due to the low viscosity of the epoxy used in this study, the epoxy was well impregnated into the rGO aerogel. The thermal conductivity of the epoxy/rGO composite is 0.30 W/m·K and the enhancement of the thermal conductivity compared to the neat epoxy (correspond to the 0.24 W/m·K) was only 25 % and it is similar to that of the epoxy/rGO composite prepared by using conventional solution mixing in the literature [16]. This result indicated that three-dimensional heat transfer pathway play the minor role in determining the effective thermal conductivity of carbon/polymer composite.

4.3.3. Thermal Conductivity of Core-Shell Structured Epoxy/rGO Aerogel

The infiltration time of epoxy plays a significant role in determining volume fraction of the rGO aerogel core in the core-shell structured epoxy/rGO composite. There are two samples prepared in present study; infiltration time of sample 1 was 3 minutes and sample 2 was 10 minutes. The density and volume fraction of rGO aerogels were calculated from those dimension and weight. The dimension and physical properties of two samples were summarized in Table. 4.1. Fig. 4.2 shows the temperature distribution as a function of time of the

prepared samples. This result revealed that the temperature of the samples was increasing with respect to time and reached at steady state after 300 seconds. The temperature distribution as a function of time and the converged temperature is related to the effective thermal conductivity of each sample. The effective thermal conductivity was calculated from following equation.

$$k_{eff}\frac{A_{top}}{L}(T_{bot}-T_{top}) = -hA_{top}(T_{ext}-T_{top}) - hA_{side}(T_{ext}-T_{side}), \quad (4.1)$$

where T_{bot} is the temperature of bottom surface of sample, T_{top} is the temperature of top surface of sample, T_{side} is the temperature of side surface of sample, T_{ext} is the external temperature and h is the heat transfer coefficient. In order to determine the heat transfer coefficient of two samples, finite element analysis was carried out by using COMSOL software. The geometry of core-shell structured epoxy/rGO composite was constructed based on the morphology observed by SEM and the volume fraction of each sample estimated from the density of the samples, resulting in the cylindrical-shaped geometry shown in Fig. 4.3. The numerically estimated temperature distribution as a function of time, which is shown in Fig. 4.4, was fitted to the experimentally measured temperature distribution. This result indicated that the heat transfer coefficient, estimated from the numerical simulation, is a suitable value for calculating the effective thermal conductivity of the core-shell structured epoxy/rGO composites. The theoretical model was used to estimate the effective thermal conductivity of heterogeneous composite was also studied to compare with the value obtained from equation 4.1. Tsao model which is based on the modified series and parallel models was well known analytical models to predict the effective thermal conductivity of heterogeneous composite of two materials [17]. The expression for Tsao model was given for following equation.

$$\frac{k_{eff}}{k_{epoxy/rGO}} = (1-P_2) + \frac{P_2^2}{P_2 + \left(\frac{k_{epoxy/rGO}}{k_{rGO\ aerogel}}\right)P_3}, \quad (4.2)$$

where, P_2 is the two-dimensional volume fraction of rGO aerogel

phase and P_3 is the three-dimensional volume fraction of rGO aerogel phase. The value of P_2 and P_3 was calculated by following equations.

$$P_2 = \frac{area\ occupied\ by\ phase\ rGO\ aerogel}{unit\ area}, \qquad (4.3)$$

$$P_3 = \frac{volume\ occupied\ by\ phase\ rGO\ aerogel}{unit\ volume}, \qquad (4.4)$$

The effective thermal conductivity obtained from equation 4.1 and 4.2 were listed in Table 4.2. The extremely low thermal conductivity of 0.077 W/m·K exhibited by the core-shell structured composite with 72.8 vol% rGO aerogel, considering the thermal conductivity of air (0.025 W/m·K). This result agrees well with theoretical calculation, which demonstrates that, in the case of the core-shell structured composite, the thermal insulation property of rGO aerogel strongly affects to the effective thermal conductivity of composite.

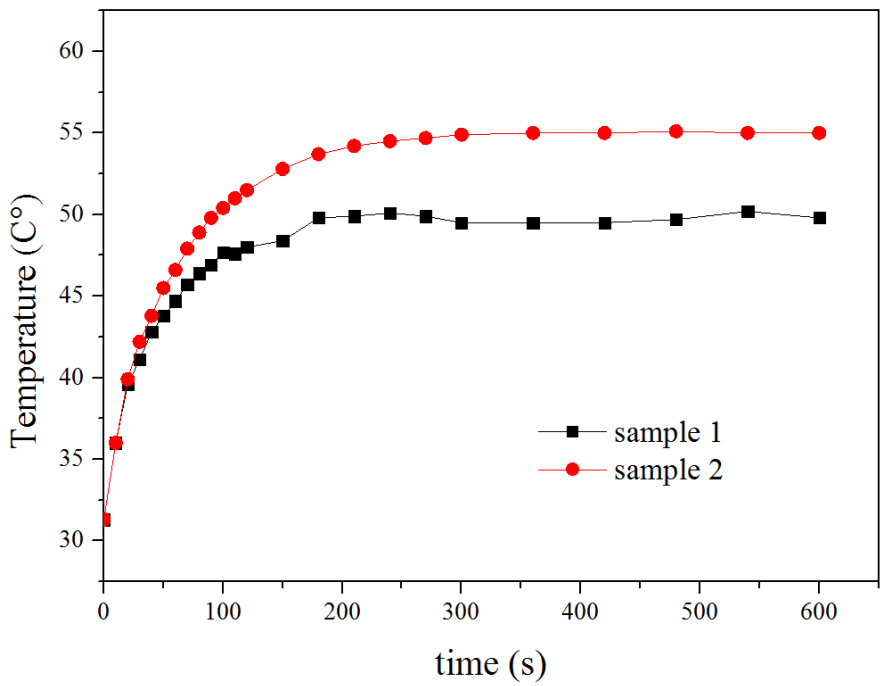

Figure 4.2. The temperature distribution as a function of time of the prepared samples

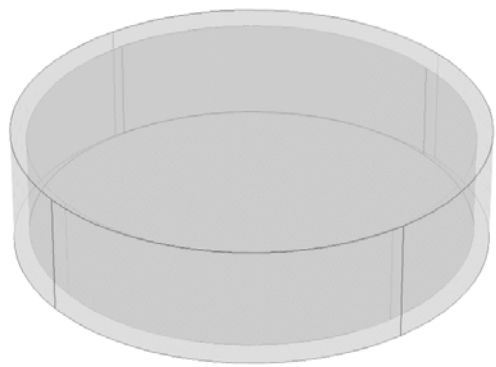

(a)

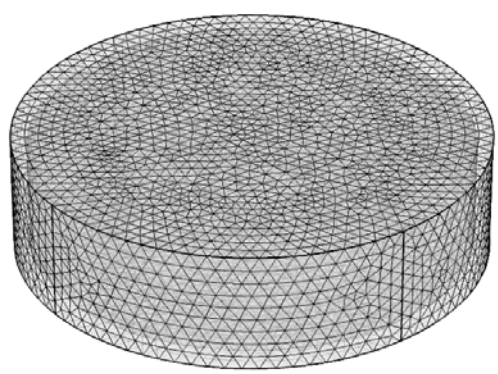

(b)

Figure 4.3. (a) The geometry and (b) three-dimensional mesh used in estimating the thermal transfer coefficient of the core-shell composite.

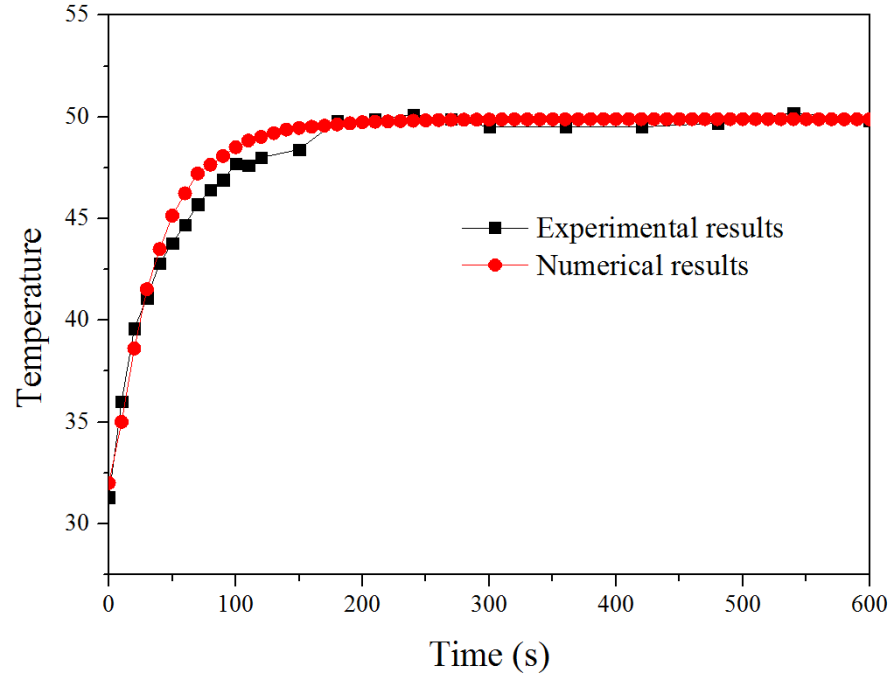

(a)

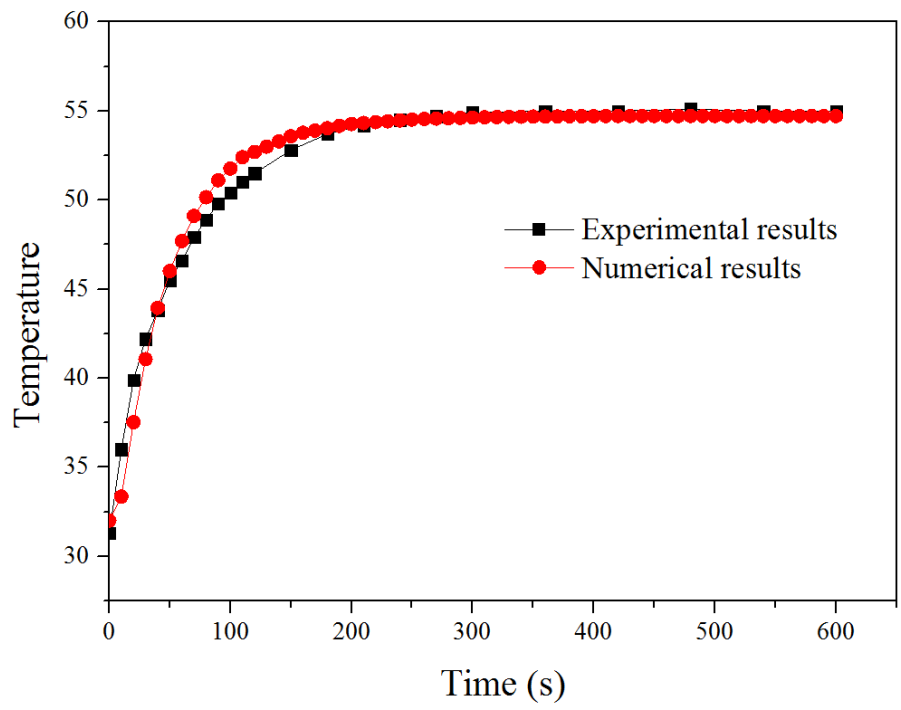

(b)

Figure 4.4. Comparison of the experiment and numerical results of (a) sample 1 and (b) sample 2.

Table 4.2. Effective thermal conductivities obtained from theoretical model and experimental results

	Sample 1	Sample 2
$k_{eff,analytical}$ (W/m·K)	0.083	0.184
k_{eff} (W/m·K)	0.077	0.165

4.3.4. Hardness of Core-Shell Structured Composite.

The Vickers hardness was calculated from following equations.

$$A = \frac{d^2}{2\sin(136°/2)} \approx \frac{d^2}{1.8544}, \quad (4.5)$$

$$HV = \frac{F}{A} \approx \frac{1.8544F}{d^2}, \quad (4.6)$$

where A is the area of applied Vickers tip, d is the distance of two different edges and F is the force which were induced by micro indentation. The Table 4.3 shows the Vickers hardness of the sample 1, the sample 2 and the neat epoxy. The hardness of sample 1 is lower than that of neat epoxy. The reason is probably that the large volume fraction of rGO aerogel in the sample 1 resulting in the decrease of resistance to the external force. In other hands, the hardness was increased in the case of sample 2. This result indicated that the hardness of epoxy composite was improved by introducing the small amount of rGO, which was accordance with the result of literature [18, 19]. Table 4.3 summarized the density and hardness of all prepared samples. The advantages of core-shell structured composite are particularly striking when the density of the prepared sample is considered. The specific hardness, defined as the ratio of hardness to specific gravity of core-shell structured epoxy/rGO composites, of prepared two samples was higher than that of neat epoxy. This means that the core-shell structured epoxy/rGO composite is suitable for weight-sensitive applications._

4.3.5. Electrical Conductivity

Electrical conductivity was also investigated in order to explore the applicability of the core-shell structured epoxy/rGO composite for the electrical applications. Although the effective thermal conductivity of the rGO aerogel was comparable to that of thermal insulating materials, the electrical conductivity of the rGO aerogel exhibits 0.8 S/m with ~0.3 vol% filler. When the epoxy resin is impregnated into the rGO aerogel, the electrical conductivity of the core-shell structured

composite was decreased to 0.4~0.6 S/m. These results were summarized in Table 4.4. It is worth noting the volume fraction of the rGO aerogel core plays a minor role in determining the electrical conductivity of composite. The electrical conductivity of core-shell structured composite is almost 10 orders of magnitude higher than that of neat epoxy. This result also proved the different mechanism of thermal and electrical transfer in carbon/polymer composites. The excellent electrical conductivity and their independence of infiltration of epoxy resin were attributed to the presence of the conductive graphene network and tunneling effect of electrical behaviors [20, 21]. However, thermal transport was governed by the phonon transfer which was also called lattice vibration [22-25]. Considering the low thermal conductivity of the epoxy/rGO composite in this study, the three-dimensional network plays the minor role in determining the effective thermal conductivity of composite.

Table 4.3. Density and hardness of prepared two samples and neat epoxy.

	Density (g/cm^3)	Hardness (HV30/10)	Specific Hardness (HV30/10)
Sample 1	0.435	10.87 ± 1.75	24.98
Sample 2	1.001	19.98 ± 0.48	19.96
Epoxy	1.145	17.92 ± 0.38	15.65

Table 4.4. Electrical conductivity of two prepared samples and rGO aerogel.

	Electrical conductivity (S/m)
Sample 1	0.505
Sample 2	0.543
rGO aerogel	0.6 ~ 0.8

4.4. Summary

The lightweight and mechanically enhanced carbon/polymer composite were prepared by constructing the core-shell structure of the aerogel core and the polymer composite shell. The specific hardness of core-shell epoxy/rGO composites was higher than that of neat epoxy. The thermal and electrical properties of core-shell epoxy/rGO composites were also investigated. The outstanding electrical conductivity of rGO aerogel was the evidence of the presence of three-dimensional conductive network in the the rGO aerogel core, resulting in the high electrical conductivity of core-shell structured epoxy/rGO composites. However, the thermal conductivity of composites and rGO aerogel is comparable to the thermal insulating materials. The reason is probably that the dominant factor to determine the effective thermal conductivity of carbon/polymer composites is not bound to three-dimensional heat transfer pathway but the interfacial thermal resistance between the polymer matrix and the carbon filler. The core-shell structured epoxy/rGO composite has the extraordinary conductivity including the extremely low thermal conductivity and high electrical conductivity. This result indicated that the core-shell structured epoxy/rGO composite would be applicable to various applications such as joule heating, thermoelectric device and *etc*.

4.5. References

[1] Bryning MB, Milkie DE, Islam MF, Hough LA, Kikkawa JM, Yodh AG. *Carbon nanotube aerogels*. Advanced Materials. 2007;19(5):661-4.

[2] Bordjiba T, Mohamedi M, Dao LH. *New Class of Carbon-Nanotube Aerogel Electrodes for Electrochemical Power Sources*. Advanced materials. 2008;20(4):815-9.

[3] Sun H, Xu Z, Gao C. *Multifunctional, ultra-flyweight, synergistically assembled carbon aerogels*. Advanced Materials. 2013;25(18):2554-60.

[4] Novoselov KS, Geim AK, Morozov SV, Jiang D, Zhang Y, Dubonos SV, et al. *Electric field effect in atomically thin carbon films*. science. 2004;306(5696):666-9.

[5] Chen T, Zeng B, Liu J, Dong J, Liu X, Wu Z, et al. *High throughput exfoliation of graphene oxide from expanded graphite with assistance of strong oxidant in modified Hummers method*. Journal of Physics: Conference Series: IOP Publishing; 2009. p. 012051.

[6] Chen J, Yao B, Li C, Shi G. *An improved Hummers method for eco-friendly synthesis of graphene oxide*. Carbon. 2013;64:225-9.

[7] Botas C, Álvarez P, Blanco P, Granda M, Blanco C, Santamaría R, et al. *Graphene materials with different structures prepared from the same graphite by the Hummers and Brodie methods*. Carbon. 2013;65:156-64.

[8] Wang X, Bai H, Yao Z, Liu A, Shi G. *Electrically conductive and mechanically strong biomimetic chitosan/reduced graphene oxide composite films*. Journal of Materials Chemistry. 2010;20(41):9032-6.

[9] Wajid AS, Ahmed H, Das S, Irin F, Jankowski AF, Green MJ. *High-Performance Pristine Graphene/Epoxy Composites With Enhanced Mechanical and Electrical Properties*. Macromolecular Materials and Engineering. 2013;298(3):339-47.

[10] Park W, Hu J, Jauregui LA, Ruan X, Chen YP. *Electrical and thermal conductivities of reduced graphene oxide/polystyrene composites*. Applied Physics Letters. 2014;104(11):113101.

[11] Zhang K, Zhang Y, Wang S. *Enhancing thermoelectric properties of organic composites through hierarchical nanostructures*. Scientific reports. 2013;3:3448.
[12] Wang W, Zhang Q, Li J, Liu X, Wang L, Zhu J, et al. *An efficient thermoelectric material: preparation of reduced graphene oxide/polyaniline hybrid composites by cryogenic grinding.* RSC Advances. 2015;5(12):8988-95.
[13] Hummers Jr WS, Offeman RE. *Preparation of graphitic oxide*. Journal of the American Chemical Society. 1958;80(6):1339-.
[14] Ha H, Shanmuganathan K, Ellison CJ. *Mechanically stable thermally crosslinked poly (acrylic acid)/reduced graphene oxide aerogels.* ACS applied materials & interfaces. 2015;7(11):6220-9.
[15] Koo MS, Chung K, Youn JR. *Reaction injection molding of polyurethane foam for improved thermal insulation*. Polymer Engineering & Science. 2001;41(7):1177-86.
[16] Tang G, Jiang Z-G, Li X, Zhang H-B, Dasari A, Yu Z-Z. *Three dimensional graphene aerogels and their electrically conductive composites*. Carbon. 2014;77:592-9.
[17] Tsao GT-N. *Thermal conductivity of two-phase materials. Industrial & Engineering Chemistry*. 1961;53(5):395-7.
[18] Tripathi SN, Saini P, Gupta D, Choudhary V. *Electrical and mechanical properties of PMMA/reduced graphene oxide nanocomposites prepared via in situ polymerization.* Journal of Materials Science. 2013;48(18):6223-32.
[19] Layek RK, Samanta S, Nandi AK. *The physical properties of sulfonated graphene/poly (vinyl alcohol) composites*. Carbon. 2012;50(3):815-27.
[20] Hu N, Karube Y, Yan C, Masuda Z, Fukunaga H. *Tunneling effect in a polymer/carbon nanotube nanocomposite strain sensor*. Acta Materialia. 2008;56(13):2929-36.
[21] Hu N, Karube Y, Arai M, Watanabe T, Yan C, Li Y, et al. *Investigation on sensitivity of a polymer/carbon nanotube composite strain sensor*. Carbon. 2010;48(3):680-7.
[22] HASSELMAN, D. P. H.; JOHNSON, Lloyd F. *Effective thermal conductivity of composites with interfacial thermal barrier resistance.*

Journal of Composite Materials, 1987, 21.6: 508-515.
[23] NAN, Ce-Wen, et al. *Effective thermal conductivity of particulate composites with interfacial thermal resistance*. Journal of Applied Physics, 1997, 81.10: 6692-6699.
[24] YU, W.; CHOI, S. U. S. *The role of interfacial layers in the enhanced thermal conductivity of nanofluids: a renovated Maxwell model*. Journal of Nanoparticle Research, 2003, 5.1-2: 167-171.
[25] ZHONG, Hongliang; LUKES, Jennifer R. *Interfacial thermal resistance between carbon nanotubes: molecular dynamics simulations and analytical thermal modeling*. Physical Review B, 2006, 74.12: 125403.

Chapter. 5. Conclusion Remarks

This study is aimed to investigate the thermal behavior of various lightweight carbon/polymer composites and comprehend the dominant factor to determine thermal conductivity of composites. On the basis of understanding the roles of factors which affects the thermal behavior of composite, the application of carbon/polymer composite can be expanded.

The injection moldable and thermally conductive thermoplastic PPS/BN composites were prepared by using injection molding machine. Thermal conductivity of the PPS/BN composite was enhanced with increasing the weight fraction of thermally conductive filler. The PPS/BN/MWCNT composites were also prepared by adding 1wt% MWCNT for further enhancement of thermal conductivity. The expected role of MWCNTs was the bridge material for the BN fillers to construct the three-dimensional heat transfer pathway and the thermal interface materials to reduce the interfacial thermal resistance between the PPS matrix and the BN fillers. The synergistic improvement of thermal conductivity was observed in the PPS/BN/MWCNT. However, three-dimensional network composed of MWCNT and BN was rarely seen in the PPS/BN/MWCNT composite. This is evidence that the effect of 3D heat transfer pathway was insignificant to increase the effective thermal conductivity of the PPS/BN/MWCNT composite. From the characterization results of surface treated MWCNT, it is evident that the hydroxyl functional groups and the carboxyl functional groups were observed mainly on the surface of hydrogen peroxide treated MWCNT and acid treated MWCNT, respectively. This result indicated that different functionality of surface treated MWCNT affected the interfacial interaction between the PPS matrix and BN matrix. The quantitative analysis was carried out by using numerical analysis with representative volume element. The numerical analysis was employed to estimate the interfacial thermal resistance of surface treated MWCNT composites. The numerical results agree well with the

experimental characterization results of the surface treated MWCNT composites. This is further evidence that the main role of MWCNT was to manipulate the interfacial thermal resistance between PPS matrix and BN filler. This result also demonstrated that lightweight and thermally conductive carbon/polymer composites could be fabricated by reducing the interfacial thermal resistance of carbon/polymer composites.

In the study of the GNP embedded PVA aerogel, thermal and mechanical behavior of carbon aerogel were investigated in various experimental conditions. Three-dimensional GNP/PVA aerogel was fabricated by using freeze-drying method allowing the simple modification to the internal structure of carbon aerogel. In order to control the internal structure of composite aerogel, different solvent composition and chemical treatment to the aerogels were applied. The addition of ethanol to DI water resulted in more stable dispersion of GNPs in the solvent and the formation of smaller pores. However, the thermal conductivity of the GNP/PVA aerogels are very low and their thermal conductivity was not depended on the formation of three-dimensional network but the porosity of composite aerogel. This implied that the role of thermal transfer network was not essential to determine the thermal conductivity of composite aerogel. On the other hand, the internal structure of composite aerogel strongly affects the thermal conductivity, mechanical property and the stability in the aqueous environment. This study was expected to provide a simple way of controlling the physical properties of carbon aerogel and expands its fields of application.

The three dimensional network was also observed in the core-shell structured epoxy/rGO composite. The formation of conductive transfer network was demonstrated by the electrical conductivity measurement of the core-shell structured epoxy/rGO composites. However, the effective thermal conductivity of the core-shell structured epoxy/rGO composites was comparable to that of the thermal insulating materials. Thermal conductivity of the epoxy/rGO aerogel composite fabricated by using vacuum infiltration was also measured. However,

enhancement in the thermal conductivity was only 25%, which was similar to the thermal conductivity of epoxy/rGO composite fabricated by using conventional solution mixing. This result implied that the effective thermal conductivity of composite was governed by interfacial thermal resistance. Considering the lightweight of the rGO aerogel core and the high specific hardness of the epoxy/rGO composite shell, this unique carbon/polymer composite has a great potential for a lot of applications including the thermoelectric device and EMI shielding.

We anticipate that the distinctive features of various carbon/polymer composites noted here and comprehensive investigation of the dominant factor to determine the thermal conductivity will help exploring the new attractive lightweight carbon/polymer composite applications.

Korean Abstract

본 연구는 탄소 고분자 복합재료의 열 전달 거동에 관한 이해와 복합재료의 열 전달 거동에 영향을 끼치는 요인의 분석을 목표로 설정하였다. 3차원 구조 열 전달 통로의 형성과 열 계면 저항은 복합재료의 열 전달 거동에 크게 영향을 끼칠 수 있는 요인으로 알려져 있다. 이 두 가지 요인의 역할을 2장과 3장에서 집중적으로 분석하였고, 4장에서는 독특한 열 적, 전기적 특성을 가지고 있는 코어-쉘 구조 탄소 고분자 복합재료에 대해 연구하였다. 또한 본 연구의 실험결과를 바탕으로 탄소 고분자 복합재료의 가벼운 특성을 살릴 수 있는 다양한 활용분야에 관한 연구를 진행하였다.

2장에서는 폴리(페닐린 설파이드)/보론 나이트라이드/탄소나노튜브(PPS/BN/MWCNT) 복합재료의 열 전달 거동을 연구하였으며, 한 종류의 충전제를 사용한 복합재료보다 두 종류의 충전제를 사용한 복합재료의 열전도도가 크게 증가하는 것이 관찰되었다. 이 공동 상승 효과에 대한 원인을 앞서 언급한 두 가지 요인으로 가정하여 연구를 수행하였다. 전자 현미경으로 관찰한 복합재료 내부구조의 형태학 분석에서 MWCNT와 BN으로 이루어진 3차원 열 전달 통로가 관찰되었으나 발견 빈도가 높지 않았다. 이 결과로 열전도도의 급격한 상승의 주된 원인이 3차원 열 전달 통로의 형성이 아니라는 결론을 내릴 수 있었다. 또한 MWCNT의 표면처리로 PPS/BN/MWCNT 복합재료의 열전도도가 크게 변하는 것을 확인하였고 그 원인에 대한 분석을 진행하였다. 그 결과, 복합재료의 열전도도는 MWCNT의 표면에 생긴 기능기에 큰 영향을 받으며, 이를 통해 MWCNT가 BN과 PPS사이의 열 계면 저항에 영향을 준다고 추론하였다. RVE를 이용한 수치해석은 이러한 추론에 대한 근거로 제시되었다. 본 연구에서 제작한 PPS/BN/MWCNT는 사출성형이 가능하며 낮은 열전도도에 비해 높은 방열특성을 가지고 있으므로 전기장치의 방열구조에 활용 가능성이 높다. 또한 고분자 복합재료의 장점인 가벼운 무게를 고려하면 현재 방열재료로 주로 이용되는 금속을 대체하는 재료로서 활용될 수 있

을 것으로 기대된다.

3장에서는 그래파이트 나노플레이트렛/폴리(비닐 알코올) (GNP/PVA) 에어로겔에 관한 연구를 수행하였다. 높은 열전도성을 가지고 있는 GNP 충전제를 사용하여 3차원 구조의 에어로겔을 제작하였고, GNP/PVA 에어로겔의 내부 구조를 두 가지 방법으로 제어하였다. 먼저, 에어로겔 제작 과정에서 사용하는 용매의 구성에 변화를 주어 내부 구조를 제어하고자 하였으며, 또 다른 제어방법으로 maleic acid를 첨가하여 PVA의 가교 현상을 유도하였다. 극저온 동결 주사 현미경 분석 결과, 용매 구성의 변화는 동결 상태에서 용매의 얼음 결정 형성에 영향을 주어 에어로겔의 내부구조를 변화시킴을 확인할 수 있었다. Maleic acid의 첨가로 인한 PVA의 가교현상은 FT-IR과 FE-SEM으로 확인되었고 에어로겔의 내부구조의 변화를 확인하였다. 열전도도 분석 결과, GNP/PVA 에어로겔의 내부구조가 변화함에 따라 에어로겔의 열전도도 역시 변화하였다. 또한 에어로겔의 역할적 성질과 수분 환경에서의 안정성이 에어로겔의 내부구조의 형태로 인해 변화되었음을 확인할 수 있었다. 본 연구에서는 간단한 방법으로 탄소 에어로겔의 물리적 성질을 제어할 수 있음을 실험적으로 증명하였으며 이 결과를 바탕으로 탄소 에어로겔 활용분야의 확장이 기대된다.

4장에서는 바인더 재료를 이용하지 않는 그래핀 에어로겔을 제작하였으며 그래핀 에어로겔의 특징인 낮은 밀도를 활용하는 동시에 에어로겔의 취약한 표면 경도를 극복할 수 있는 구조로 코어-쉘 구조를 제안하였으며 에폭시/환원 그래핀 옥사이드 (Epoxy/rGO) 에어로겔을 이용하여 복합재료를 제작하였다. 이 복합재료는 rGO 에어로겔의 낮은 열전도도와 높은 전기전도도를 보유하고 있으며, 코어-쉘 구조로 인해 가벼우면서도 높은 표면 경도를 보유함을 확인하였다. 본 연구에서 제안한 코어-쉘 구조를 이용한다면 향후 탄소 고분자 복합재료의 활용성이 증가할 것으로 기대된다.

주요어: 탄소 고분자 복합재료, 열전도도, 열 계면 저항, 3차원 열 전달 통로, 탄소 에어로겔, 코어−쉘 구조
학번: 2008−20644